

---


Electronic Theses and Dissertations, 2004-2019

---

2016

## Forced Convection Cooling of Electric Motors Using Enhanced Surfaces

Mohammed Almaghrabi  
*University of Central Florida*

 Part of the [Mechanical Engineering Commons](#)  
Find similar works at: <https://stars.library.ucf.edu/etd>  
University of Central Florida Libraries <http://library.ucf.edu>

This Masters Thesis (Open Access) is brought to you for free and open access by STARS. It has been accepted for inclusion in Electronic Theses and Dissertations, 2004-2019 by an authorized administrator of STARS. For more information, please contact [STARS@ucf.edu](mailto:STARS@ucf.edu).

---

### STARS Citation

Almaghrabi, Mohammed, "Forced Convection Cooling of Electric Motors Using Enhanced Surfaces" (2016). *Electronic Theses and Dissertations, 2004-2019*. 5272.  
<https://stars.library.ucf.edu/etd/5272>

FORCED CONVECTION COOLING OF ELECTRIC MOTORS USING  
ENHANCED SURFACES

by

MOHAMMED ALMAGHRABI

B.S. University of South Florida, 2011

A thesis submitted in partial fulfillment of the requirements  
for the degree of Master of Science  
in the Department of Mechanical and Aerospace Engineering  
in the College of Engineering and Computer Science  
at the University of Central Florida  
Orlando, Florida

Fall Term

2016

Major Professor: Louis Chow

© 2016 Mohammed Almaghrabi

## ABSTRACT

Electric motors are extensively engaged in industrial and commercial applications such as electrical cars, energy-conversion systems, elevators, and actuators for aircrafts. Due to the significant internal heat generation, it is usually a challenge to design and manufacture high power density, high reliability, and low cost electric motors with superior performance. One of the efficient ways to dissipate the heat generated in the electrical motor is by using extended surfaces (i.e. heat sinks). These surfaces are extruded from the motor casing and air is forced through them by a cooling fan. This cooling approach is simple to be implemented and has zero carbon emission to the environment. Adding ribs on the motor extended surface enhances the heat dissipation rate. This project is intended to study numerically the effect of varying ribs spacing and ribs heights on heat removal efficiency, accounting for the relative change in heat transfer coefficient and pressure drop compared to those for a smooth flow channel. The study is conducted to simulate the airflow field, and heat transfer for a plate heat sink using ANSYS V.16.

The domain considered in the present work is a simple design of an electric motor annulus. The electric motor annulus consists of an array of ribbed fins. Heat source is represented as a uniform heat flux of  $12250 \text{ W/m}^2$  at the bottom surface of the heat sink base. Through the simulations, the rib heights ( $e=0.05, 0.1, 0.2$ , in mm) and spacing ( $p=1, 2,3,4,5$ , in mm) between the ribs, the channel width ( $W_{ch}= 2$  and  $6$  in mm), and the rib configuration

(continues and inline ribs) are varied to study their effect on the performance of the heat sink for a Reynolds number range from 3133 to 12532.

To assess which rib configuration is best, a figure of merit (named as thermal-hydraulic performance) is used which is defined as the ratio of heat transfer enhancement to the increase in pumping power due to the presence of the ribs. The highest thermal-hydraulic performance value out of all the transverse cases at  $W_{ch}=2$  mm in this study was 1.07 at  $e=0.05$  mm,  $p=4$  mm, and  $Re=3133$  which means only a 7% enhancement is obtained. These set of cases are suitable for increasing the rate of heat transfer while ignoring the pressure drop penalty. Changing the channel width to 6 mm increases the thermal-hydraulic performance by about 23%. Therefore, this channel width is used for the inline ribs configurations with seven different opening ratios (10% to 70%). The inline ribs are investigated at two different Reynolds number (3133 and 12532). At an opening ratio of 50% the highest thermal-hydraulic performance of 1.18 and 1.22 were found at  $Re=3133$  and  $p=5$  mm, and at  $Re=3133$  and  $p=1$  mm, respectively. These simulation results show that with proper channel and ribs configuration, one can achieve about 22% increase in the thermal-hydraulic performance ratio over that of the smooth channel.

*This thesis is dedicated to my great father and great mother*

*for their endless love and support throughout my life.*

*To my brothers and sisters for giving me the strength to chase my dreams.*

*To my dear wife and my two little angles for standing beside me during the challenges of  
graduate school and life.*

*Your endless love and care will never be forgotten*

## ACKNOWLEDGMENTS

First and above all, I praise Allah, the almighty for providing me this opportunity and granting me the capability to proceed successfully.

I would like to take this opportunity to express my gratitude and appreciation to my advisor **Dr. Louis Chow** for his continuous support, guidance, and patience throughout this study. I also would like to thank my committee members **Dr. Allain Kassab** and **Dr. Tuhin Das** for their beneficial comments, discussions, and support.

I am grateful to all my colleague who supported me, especially **Dr. Osama Meselhy**, **Engr. Ramy Abdelhady**, and **Engr. Mohammed Abdelkareem**, who have made this life-changing opportunity possible for me. Thank you for your generous comments, advises, and contributions in editing my thesis. Your friendships make my life a wonderful experience.

My deep gratitude goes to my family; my parents, sisters, brothers, and wife for their sincere encouragement, patience and prayers. Without your incredible support, this would not have been possible.

# TABLE OF CONTENTS

LIST OF FIGURES .....	x
LIST OF TABLS .....	xiii
LIST OF ACRONYMS .....	xiv
CHAPTER 1 INTRODUCTION.....	1
1.1 Background .....	2
1.2 Motor Power Losses .....	5
1.3 Motor Cooling.....	6
1.4 Motivation.....	11
1.5 Scope of Present Work.....	12
1.6 Objectives and Approach.....	12
1.7 Thesis Outline .....	13
CHAPTER 2 LITERATURE REVIEW.....	15
2.1 Introduction.....	15
2.2 Previous work .....	15
2.3 Summary .....	26
CHAPTER 3 NUMERICAL MODELING.....	28



3.1	Governing Equations .....	28
3.1.1	Continuity Equation .....	29
3.1.2	Momentum Equation.....	29
3.1.3	Energy Equation.....	30
3.1.4	Auxiliary Equations .....	31
3.1.5	General Form of Equations .....	31
3.2	Turbulence Models .....	32
3.2.1	Standard k- $\epsilon$ Model .....	32
3.2.1	Empirical Constants Used in the k- $\epsilon$ Model.....	34
3.3	Near-Wall Treatment for Turbulent Flows.....	36
3.3.1	The Standard Wall Function .....	39
3.4	Numerical Methods.....	42
3.5	Problem Description and Modeling.....	43
3.5.1	Model Description.....	43
3.5.2	Grid Generation.....	47
3.5.3	Boundary Conditions .....	49
3.6	Solver and calculations .....	50

3.7	Gird Sensitivity .....	53
3.8	Code Validation .....	54
CHAPTER 4 RESULTS AND DISCUSSION .....		59
4.1	BASE SMOOTH CASE PERFORMANCE.....	59
4.2	Transverse Ribs.....	61
4.2.1	Effect of Rib Pitch and Height .....	62
4.2.2	Effect of the Inline Ribs .....	69
CHAPTER 5 CONCLUSION .....		75
LIST OF REFERENCES.....		79

## LIST OF FIGURES

Figure 1.1: Distribution of Power Losses in Electric Motors [4].	6
Figure 1.2: Finned-Plate Heat Sink Types.	8
Figure 1.3: Technology selection guide [17].	10
Figure 3.1: Typical velocity and shear distribution in turbulent flow near the wall [78].	37
Figure 3.2: Subdivisions of the Near-Wall region [78].	38
Figure 3.3: Near-wall treatments in FLUENT [78].	39
Figure 3.4: Problem set-up flow chart.	43
Figure 3.5: Electric motor annulus with ribbed fins.	45
Figure 3.6: Computational domain, (a) continuous ribs configuration, (b) inline ribs configuration.	46
Figure 3.7: Structured and hexahedral mesh for the present heat sink.	49
Figure 3.8: Variation of Nusselt number with the number of mesh elements.	54
Figure 3.9: The ribbed channel model with a rib angle of 30°.	55
Figure 3.10: Comparison of the Numerical results with [22] experimental results.	57
Figure 4.1: Variation of the Average Nusselt Number with Reynolds Number for the Base Smooth Case Performance.	60
Figure 4.2: Variation of the Friction Factor with Reynolds Number for the Base Smooth Case Performance.	61

Figure 4.3 Velocity Contour over the case where $p=5$ mm, $e=0.2$ mm, and $Re=3133$ .....	62
Figure 4.4: Variation of the average Nusselt number ratio with Reynolds number for a fixed value of $e=0.05$ mm and different values of $p$ (in mm).....	63
Figure 4.5: Variation of the average Nusselt number ratio with Reynolds number for a fixed value of $e=0.1$ mm and different values of $p$ (in mm).....	64
Figure 4.6: Variation of the average Nusselt number ratio with Reynolds number for a fixed value of $e=0.2$ mm and different values of $p$ (in mm).....	64
Figure 4.7: Variation of the average friction ratio with Reynolds number for a fixed value of $e=0.05$ mm and different values of $p$ (in mm).....	65
Figure 4.8: Variation of the average friction ratio with Reynolds number for a fixed value of $e=0.1$ mm and different values of $p$ (in mm).....	65
Figure 4.9: Variation of the average friction ratio with Reynolds number for a fixed value of $e=0.2$ mm and different values of $p$ (in mm).....	66
Figure 4.10: Variation of the thermal-hydraulic performance with Reynolds number for a fixed value.....	66
Figure 4.11: Variation of the thermal-hydraulic performance with Reynolds number for a fixed value of $e=0.1$ mm and different values of $p$ (in mm).....	67
Figure 4.12: Variation of the thermal-hydraulic performance with Reynolds number for a fixed value of $e=0.2$ mm and different values of $p$ (in mm).....	67
Figure 4.13: Evaluation of the average Nusselt number correlation.....	69

Figure 4.14: Variation of the average Nusselt number ratio with the opening ratio at P=5 mm and two different Reynolds numbers.....	71
Figure 4.15: Variation of the average friction ratio with the opening ratio at P=5 mm and two different Reynolds numbers.....	72
Figure 4.16: Variation of the thermal-hydraulic performance ratio with the opening ratio at P=5 mm and two different Reynolds numbers. ....	72
Figure 4.17: Variation of the average Nusselt number ratio with the opening ratio at P=1 mm and two different Reynolds numbers.....	73
Figure 4.18: Variation of the average friction ratio with the opening ratio at P=1 mm and two different Reynolds numbers.....	73
Figure 4.19: Variation of the thermal-hydraulic performance ratio with the opening ratio at P=1 mm and two different Reynolds numbers. ....	74

## LIST OF TABLES

Table 1.1: Statistics Obtained from IEEE and EPRI motor reliability surveys [5].....	4
Table 1.2: Ranges of heat transfer coefficients [18]. .....	10
Table 3.1: Diffusion coefficient and source terms for variable $\Phi$ [79]. .....	35
Table 3.2: Empirical constants used in the k- $\epsilon$ model [78]. .....	35
Table 3.3: Heat sink parameters .....	47
Table 3.4: Comparison between the present numerical results and the experimental results [22].....	58
Table 4.1: Values of the Parameters Considered in the Base Smooth Case .....	60

## LIST OF ACRONYMS

Symbol	Definition
$A_c$	Cross sectional area of the channel, [m <sup>2</sup> ]
$C_p$	Specific Heat at Constant Pressure, [J/kg .K]
$C_{\epsilon 1}$ & $C_{\epsilon 2}$	Model Constants for the Turbulence Model
$C_{\mu}$ & $C_D$	Model Constants for the Turbulence Model
$D_h$	Channel Hydraulic Diameter, [m]
$D_m$	Motor Diameter, [m]
$E$	Turbulent Dissipation Rate, [m <sup>2</sup> /s <sup>5</sup> ]
$H$	Fin Height, [mm]
$JF$	Thermal-hydraulic performance
$L$	Length Scale of Turbulence, [m]
$L_{ch}$	Channel Length, [mm]
$N$	Number of Opening through the Solid Rib
$\overline{Nu_r}$	Average Nusselt Number for the Ribbed Case
$Nu_{s,fd}$	Nusselt Number for the Fully Developed Smooth Case
$Nu$	Nusselt Number Using $D_h$ as a Characteristic Length
$P$	Channel pressure, [N/m <sup>2</sup> ]
$PP$	Pumping Power
$P_r$	Prandtl Number
$P_{rt}$	Turbulent Prandtl Number
$Q$	Heat Input, [W]
$Re_{D_h}$	Reynolds Number Using $D_h$ as a Characteristic Length
$S_u$	Source Term, [N/m <sup>3</sup> ]
$T_i$	Inlet Temperature, [K]
$T_m$	Mean Air Temperature, [K]
$T_p$	Temperature at the Cell Adjacent to Wall, [K]
$T_w$	Temperature at the Wall, [K]

$U_c$	Mean Velocity Magnitude at $y^* = y_T^*$ , [m/s]
$U_p$	Mean Velocity of the Fluid at Point $P$ , [m/s]
$V$	Volumetric Flow rate
$W_{ch}$	Width Length, [mm]
$W_{ch}$	Channel Width, [mm]
$k_t$	Turbulent Thermal Conductivity, [W/m.K]
$u^+$	Dimensionless Velocity
$u_t$	Wall Friction Velocity ( $=\sqrt{\tau_w / \rho}$ ), [m/s]
$y$	Normal Distance to the Wall, [m]
$y^+$	Dimensionless Wall Distance.
$u', v', w'$	Fluid Fluctuating Velocities, [m/s]
$\bar{f}_r$	Average friction factor for the ribbed case
$f_{s,fd}$	Friction Factor for the Fully Developed Smooth Case
$u_i$	Absolute Velocity in the $i^{th}$ Direction, [m/s]
$x_i$	Coordinate in the $i^{th}$ Direction
$a$	Fin Thickness, [mm]
$b$	Base Plate Height, [mm]
$c^+$	an Empirical Constant ( $c^+ = 5.45$ )
$e$	Rib Height, [mm]
$f$	Friction factor
$h$	Convection Heat Transfer Coefficient, [W/m <sup>2</sup> .K]
$k$	Thermal Conductivity of a Heat Sink Material, [W/m.K]
$K_c$	the Von Karman Constant
$k_{eff}$	Effective Thermal Conductivity, [W/m.K]
$k_l$	Laminar Thermal Conductivity, [W/m.K]
$k_t$	Turbulence Kinetic Energy, [m <sup>2</sup> /sec <sup>2</sup> ]
$p$	Rib Pitch, [mm]
$q$	Wall Heat Flux, [W/m <sup>2</sup> ]



$x$	Axial Coordinate, [m]	
<i>Greek symbols</i>		
$\alpha$	Thermal Diffusivity, [m <sup>2</sup> /sec]	
$\tau$	Shear Stress, [N/m <sup>2</sup> ]	
$\theta$	Inclination Angle of the Rib, [degree]	
$\sigma_k$ & $\sigma_\varepsilon$	Model Constants for the Turbulence Model	-
$\Delta P$	Pressure Drop across Heat Sink, [N/m <sup>2</sup> ]	
$\Delta T$	Temperature Difference, [K]	
$\mu_{eff}$	Summation of the Laminar and the Turbulent Viscosity, [Pa.s]	
$\mu_l$	Laminar Dynamic Viscosity, [Pa.s]	
$\mu_t$	Turbulent or Eddy Viscosity, [Pa.s]	
$p$	Channel Perimeter, [m]	
$\delta_{ij}$	the Kronecker Delta	
$\varepsilon$	Turbulent Dissipation Rate, [m <sup>2</sup> /sec <sup>5</sup> ]	
$\mu$	Dynamic viscosity, [Pa.s]	
$\nu$	Kinematic Viscosity, [m <sup>2</sup> /sec]	
$\rho$	Density, [kg/m <sup>3</sup> ]	
$\tau_w$	Wall Shear Stress, [N/m <sup>2</sup> ]	
$\Gamma_k$	Diffusion Coefficient for Turbulent Kinetic Energy	
$\Gamma_\varepsilon$	Diffusion Coefficient for the Dissipation of Turbulent Kinetic Energy	
<i>Subscripts:</i>		
a	Ambient, Absolute, Air.	
b	Base Plate	
ch	Channel	
D <sub>h</sub>	Hydraulic Diameter	
eff	Effective	
f	Friction	
i	Term Number, Tensor Index (1, 2, 3).	
i	Inlet	

<i>PP</i>	Pumping Power
<i>r</i>	Ribbed case
<i>s,fd</i>	Fully Developed Smooth Case
<i>w</i>	Wall
<i>X</i>	Component in x-Direction.
<i>Y</i>	Component in y-Direction.
<i>Z</i>	Component in z-Direction.

*Superscripts:*

-	Time Averaged Value
'	Fluctuating Component

*Abbreviations:*

2D	Two Dimension.
3D	Three Dimension.
CFD	Computational Fluid Dynamics
EPRI	Electric Power Research Institute
FVM	Finite Volume Method
IEEE	Institute of Electrical and Electronics Engineers
OR	Rib Opening Ratio
RNG	Reynolds Normalized Group
SIMPLE	Semi-Implicit Method for Pressure-Linked Equations
SISE	Side Inlet Side Exit

## **CHAPTER 1      INTRODUCTION**

An electric motor is a machine that converts electric energy into mechanical energy. It is one of the most imperative applications of electromagnetism. A magnetic field is generated inside the motor by the flow of the electric current that passes through the coils (winding currents). To derive an external load, a motor torque is generated from the interaction between the stator and the rotor magnetic fields. A classic electric motor consists of a rotor, a stator, end bells, a shaft, bearings, and a motor housing. Other electric motor configurations may include more components. It can be found in a range of applications such as electronic products, industrial drives, electric vehicles, machine tools, robots, and space-crafts. Nowadays, systems that are driven by an electric motor form approximately 45% of the aggregate electricity consumption in the globe [1]. In the near future, energy consumption from electric motors is expected to increase to 13,360 terawatt hour (TWh) annually. In other words, electricity consumptions from electric motor driven systems costs end-users around USD 565 billion annually; eventually, that could increase to USD 900 billion [1]. The motor driven systems in the industries sector in the United States consume 64% of the electricity. The electricity consumption is around 290 billion kilowatt hours (kWh) of power per year [2]; more than 40% of the electric motors are used in industrial processes [3]. Moreover, energy cost is a crucial part of the electric motor's life cycle and it represents 95% of it [4].

Due to the rapid increase on energy demands and its costs around the globe, most of the motors manufacturers focus on energy consumption reduction to increase the motor efficiency through implementation of advanced technology. The efficient way to dissipate the heat generated on the electrical motor is using the extended surfaces (i.e. heat sinks). These surfaces are extruded from the stator and air is drawn through them by a cooling fan. This way is simple to be manufactured and implemented and has zero carbon emission to the environment.

### 1.1 Background

There are many reasons that cause the failure of electric motors. The most common failure modes are electrical failure and mechanical failure. This study only focuses on the electrical failure, which occurs most of the time, because of the exceeding of the temperature limit of the winding which causes the winding insulation to breakdown. There are other issues that could cause the breakdown of the winding insulation such as overloading condition and winding short circuits [4].

Data revealed that the approximate annual motor failure percentage is from 3% to 5% and sometimes could go up to 12% like in the paper and pulp industry [5]. Motor failure is very costly in industry and sometimes it could be costlier than the replacement of the motor itself. Not only that, it also could cause disruption on the production line, which will increase the total lost cost [4].

A three part report was published by the Institute of Electrical and Electronics Engineers (IEEE) Motor Reliability Working Group to show the motor failure modes based on the root cause of failure [6-8]. A comparable study by the Electric Power Research Institute (EPRI) showed results based on mechanical failure of components [9]. The two results were compared in Table 1.1 by Venkataraman et al. [5]. It can be clearly seen from the table that the most common reasons of the motor failures are the overheating from the overload which will cause total failure to the engine or shorten the life time of the stator insulation. Therefore, most of the motor failure modes are associated directly or indirectly with the excessive operation temperature.

Table 1.1: Statistics Obtained from IEEE and EPRI motor reliability surveys [5].

IEEE Survey		EPRI Survey		Average %
Failure Contribution	%	Failure Contribution	%	Electrical Related Failure  33.3%
Persistent Overload	4.2%	Stator Ground Insulation	23%	
Normal Deterioration	26.4%	Turn Insulation	4 %	
		Bracing	3%	
		Core	1%	
		Cage	5%	
Electrical Related Total	30.6%	Electrical Related Total	36%	Mechanical Related Failure  31.35%
High Vibration	15.5%	Sleeve Bearings	16%	
Poor Lubrication	15.2%	Antifriction Bearings	8%	
		Trust Bearings	5%	
		Rotor Shaft	2%	
		Rotor Core	1%	
Mechanical Related Total	30.7%	Mechanical Related Total	32%	Environmental Maintenance & Other Reasons Related Failures  35.35%
High Ambient Temperature	3%	Bearing Seals	6%	
Abnormal Moisture	5.8%	Oil Leakage	3%	
Abnormal Voltage	1.5%	Frame	1%	
Abnormal Frequency	0.6%	Wedges	1%	
Abrasive Chemicals	4.2%			
Poor Ventilation Cooling	3.9%			
Other Reasons	19.7%	Other Components	21%	
Environmental Reasons and Other Reasons Total	38.7%	Maintenance Related & Other Parts Total	32%	

Knowledge of the temperature field inside the components becomes essential due to the direct relationship between operating temperatures and reliability. The cooler the electric motor operates, the more reliable it is. The focus in thermal management is then directed towards establishing cooling methods to maintain the operating temperatures below permissible temperatures prescribed by the manufacturers. According to Arrhenius equation, there is an exponential relationship between the failure rate and the operation temperature [4]. One of the major concerns thermal engineers encounter when designing a motor is the stator cooling because of different reasons. One of the reasons is that heat is

mainly generated from the stator winding. Another one is that cooling the stator end-winding region is a big challenge due to several reasons [10]. Another reason is that the cooling of the stator is less complex than the rotor [4].

## 1.2 Motor Power Losses

While the electric motor is on operation, some of the electrical energy does not transform to mechanical energy and that is defined as motor power losses. Most of the power losses transform to heat energy which causes the formation of extreme internal temperature inside the motor. Power losses could cause an increase in temperature of the winding which will reduce the efficiency of the motor. Moreover, the life time of the winding insulation is inversely proportional to the temperature. The higher the winding insulation temperature is, the less the winding insulation life time is [4].

Two power losses type's studies have been released from Benhaddadi and GE [11,12]. The following Fig. 1.1 is showing a comparison between the two different power losses investigation results from GE and Benhaddadi [11,12]. Both results revealed that most of the power losses are coming from the load losses (resistive losses from stator and rotor), and specifically from the stator winding, 35% and 33% for Benhaddadi and GE, respectively. Therefore, the no load losses, which do not necessitate load currents, form approximately 30% of the total power losses. The no load losses include magnetic losses

and mechanical losses. Magnetic losses have two types, which are hysteresis losses and eddy losses, while mechanical losses include windage and friction losses.

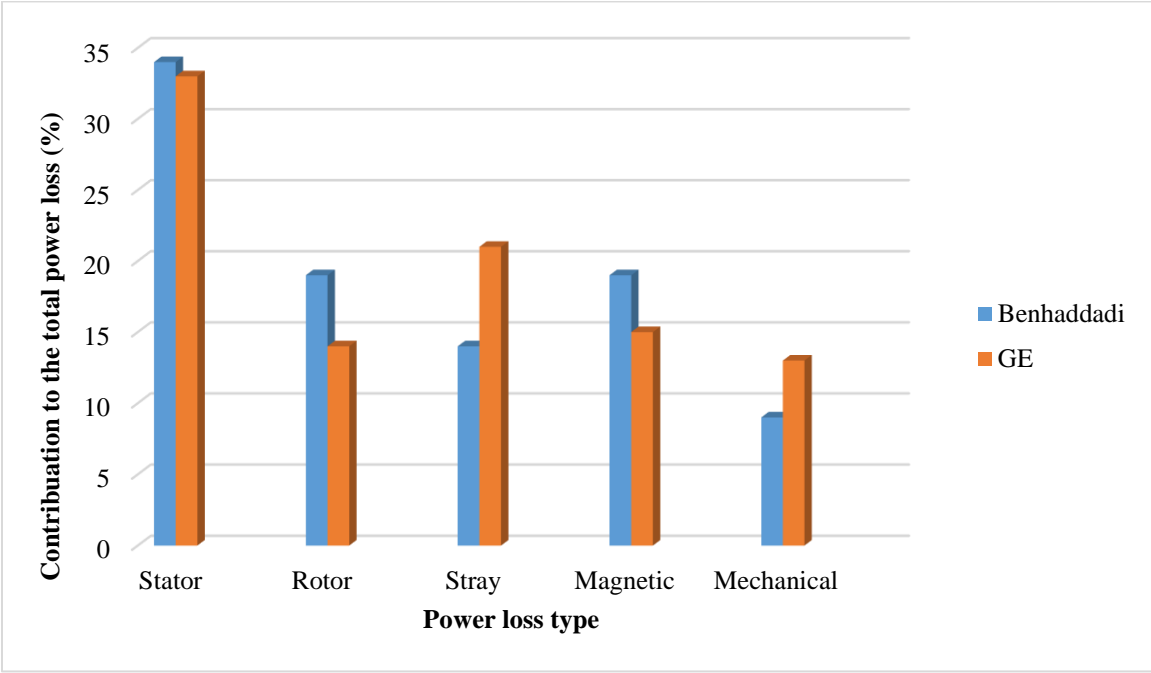


Figure 1.1: Distribution of Power Losses in Electric Motors [4].

### 1.3 Motor Cooling

Thermal management of electric motors has been one of the primary interest areas in advanced heat transfer research and development due to the need of producing more efficient, more compact, and less energy consumption motors. Heat transfer behavior inside the electric motor is complex, as heat is dissipated from the windings, conducted into the housing, and then transferred to the annulus of the motor by some combination of thermal conduction and convection.



All the power losses generated must be released from the motor to the air to assure better performance and reliability. As a result, innovative heat removal techniques have been considered in the thermal management of electric motors to keep the temperature of the stator and the rotor below the maximum prescribed limit. Liquid and phase-change cooling are two notable examples but it is very hard to implement these ways in electric motors. Air-cooling is often used since air is abundant, economical, safe, and readily available.

Increasing the airflow rate over the component and/or increasing the surface area across which convection occurs may achieve enhancement in heat transfer by air-cooling. Increasing the airflow rate requires larger blowers and often leads to higher noise levels, volume, weight, and finally greater costs. The employing of fins with a high thermal conductivity on the motor housing is used to augment the total surface area for heat dissipation. The cost of purchasing and mounting the heat sinks increases the overall cost and weight of the system. The presence of a heat sink in the system often poses an increased resistance to the airflow, and the pressure drop associated with flow then must be considered in the design. In general, it is more effective and economical to increase the surface area than the velocity.

A variety of heat sinks are available, as illustrated in Fig. 1.2. It could be either plate fins or pin fins. There are different configurations of plate fins. Such as parallel plate fin, wavy plate fin, flattered plate fin, radial–helical plate fin, and wavy protruding strip plate fins [13]. Extruded aluminum heat sinks are one form of parallel flat plate fins. They are cost

effective and relatively simple to manufacture. An array of adjacent fins forms the cooling flow channel in which the velocity profile is identical everywhere except at the entrance region. Employing ribs on the fins to roughen the surfaces will cause the separation and reattachment of the flow. The ribbed fins will disturb the flow, which will reduce the boundary layer thickness. Consequently, the heat transfer will increase due to the flow turbulence and the surface area increase. However, a price is paid for the enhancement of heat transfer in the form of pressure loss. The pressure loss through an array of square ribs increased a demand on the pumping or fan requirements of the motor.

Designing the optimal electric motor cooling system involves a tradeoff between heat transfer performance and fluid dynamic behavior. The best electric motor cooling system is not necessarily the one that rejects the most heat. The pressure drop of the flow through the mini channel of the motor annulus and the accompanying pumping requirements must be considered.



Figure 1.2: Finned-Plate Heat Sink Types.

A review of different heat transfer techniques used to accomplish electronic cooling are found in Mudawar [14], and Yeh [15]. There are different technologies available for different magnitudes of heat removal. In general, heat sinks can be categorized into five groups based on the cooling mechanism [16]:

- Passive heat sinks - generally used for applications involving natural convection cooling.
- Semi-active heat sinks - leverage off existing fans in the system.
- Active heat sinks - same principle as passive heat sinks but with the addition of a fan/blower over the heat sink, such as an impingement or side-inlet-side-exit (SISE) heat sinks, usually the case in forced convection systems; reliability is dependent on the moving parts.
- Liquid cooled cold plates - utilizes tubes in block designs or milled passages in brazed assemblies for the use of pumped water, oil, etc., as the order of complexity of different cooling mechanisms can be referred to Fig. 1.3.
- Phase Change Recirculating System -two-phase systems that employ a set of boiler and condenser in a passive, self-driven mechanism. Heat pipe systems incorporate either no wicks in a gravity fed arrangement or wicks that do not require gravity feeds [16, 17].

The following Fig. 1.3 illustrates the relationship between power dissipation and the thermal efficiency for the above discussed cooling mechanisms.

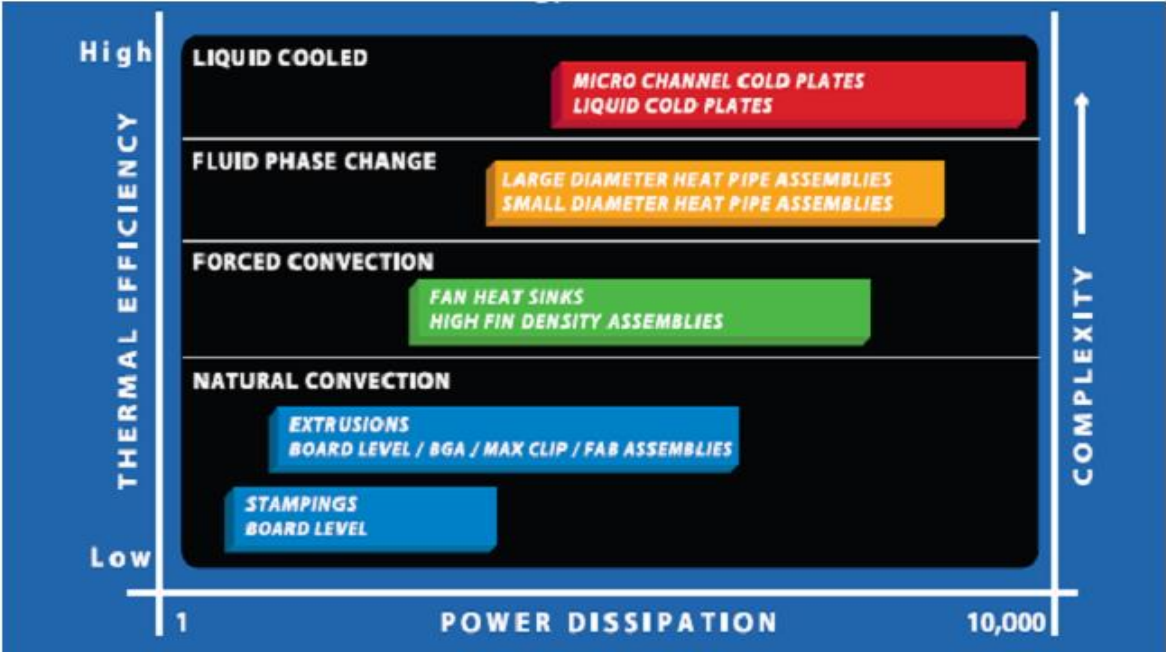


Figure 1.3: Technology selection guide [17].

Selection of the cooling method needs to begin with analytical correlations. The calculated heat transfer coefficient can be used as a preliminary parameter in the selection of cooling modes. Table 1.2 provides a guide for such a task, where the ranges of heat transfer coefficients are shown for different cooling methods and coolant fluids.

Table 1.2: Ranges of heat transfer coefficients [18].

Fluid	Method	Heat Transfer Coefficient (W/m <sup>2</sup> K)
Air	Natural Convection	3 - 12
Air	Forced Convection	10 - 100
Water	Forced Convection	3000 - 7000

Forced air cooling is being used as a viable technique for cooling electric motors. This is because of the ease of use, inherent simplicity and the availability of air. Also at the end of every cooling process, heat is normally released to the ambient air; therefore, by using an air-cooling system as primary cooling method, we can avoid the use of additional devices and consequently lower the cost.

Designs incorporating such extended surfaces typically take the form of finned heat sinks. In electric motor applications, heat sinks are directly mounted on the motor housing to provide extra surface area for heat transfer from the motor to the cooling fluid.

#### 1.4 Motivation

In the past, technologies in electric motor cooling have not developed much. Nowadays, engineers and researchers are facing many difficulties to produce a high efficient cooling system. Moreover, the performance of a heat sink depends on various factors such as the heat sink geometry, the type of the cooling fluid, and the flow properties. These parameters can significantly influence the heat sink thermal performance.

Due to the lack of information about designing electric motor cooling systems, more efforts should focus on studying various configurations of plate fin heat sinks that are used to cool down the motors. Accordingly, heat transfer and fluid flow of different heat sinks will be investigated and the effect of fin spacing, rib spacing, and rib configurations will be studied.

### 1.5 Scope of Present Work

The present work is concerned with the problem of fluid flow and heat transfer performance in the annulus of a motor where ribbed fins are mounted on the motor housing. Flow is allowed to move in the mini rectangular cross sectional channels between the ribbed fins. This project is intended to study numerically the effect of varying ribs spacing, ribs heights, and ribs configurations on heat transfer and pressure drop.

The research concentrates on the prediction of the temperature and flow field and hence the thermal and hydraulic performance of different heat sinks configurations. Computational work is also performed and comparisons are made between present work and available experimental previous works.

### 1.6 Objectives and Approach

This thesis attempts to address the heat dissipation problem of motor industries by determining the air cooling limit of a parallel plate heat sink under variable pitches and rib heights. In addition, the influence of rib configurations over the fins on the flow and heat transfer characteristics of the heat sink is investigated and analyzed. The objectives of this research are:

- Development of a computational model to predict the fluid flow and thermal performance characteristics of a plate fin heat sink with different pitches and heights.

- Validation of the model with the existing literature for thermal and hydraulic performance of a heat sink.
- Study the effect of rib pitch, rib height, and different configurations.
- Study the effect of changing Reynolds numbers.

### 1.7 Thesis Outline

This thesis consists of five chapters which are:

- Chapter one includes an introduction and background about the problem under the study. Also, the importance of the point of research and its engineering application is stressed. The motivation and the objectives of this research is presented.
- Chapter two gives a survey and analysis for the previous work of the electric and electronic cooling by using heat sink. A discussion of the previous work at the end of this chapter will route and clarify how much the importance of this study is.
- Chapter three presents an introduction to the mathematical method, the computational domain, the computational method, and the governing equations used to predict the fluid and thermal characteristics of a heat sink with variable fins height and fins spacing. Also, the grid independence study and the code validation are presented at the end of this chapter

- Chapter four contains numerical results where the data is analyzed and correlations for Nusselt number and friction factor are derived.
- Chapter five summarizes the main outcome of the study and outlines the conclusion of the numerical investigation.

The thesis comprises several tables, numerous figures and illustrations that appear within the text. In addition, a complete list of references is written at the end of the thesis.



## **CHAPTER 2      LITERATURE REVIEW**

### **2.1    Introduction**

In the last century, the convective heat transfer and pressure drop in flow channels has become a major concern for both scientists and researchers. For heat transfer rate augmentation while considering the pressure drop penalty, extended surfaces (i.e. fins) are considered one of the most common passive cooling techniques used in many engineering applications such as motors, gas turbine blades [20-23], compact heat exchangers [25-33], and electronic equipment packages [34-41].

Due to the complex nature of the flow fields, no analytical solution exists that can accurately predict plate fin array heat transfer. As a result, research has been conducted by numerous researchers to investigate how the heat transfer of parallel plate fin arrays change with geometry and flow characteristics.

### **2.2    Previous work**

The demands of compact packaging of today's advanced micro-electronic and micro-electric devices require innovative solutions to the thermal problems. Traditional heat sinks are one of the most effective techniques that are used to remove heat densities encountered in many systems. Liquid cooling (immersion, jet impingement, heat pipe etc.) is used in many applications. Many designers are trying different liquid coolants [42-51]. Although liquids have a high thermal performance, it is not preferable. Because of advantages related

to simplicity of design, operating costs and low installation as well as ease of maintenance, air cooling is still preferred. Traditional fan cooled extruded heat sinks is limited to maximum removable heat flux of about  $1 \text{ W/cm}^2$ . Thus, if air is to be retained as the coolant to satisfy the stringent requirements, one has to overcome the limitations stemming from its poor thermal conductivity. Accordingly, investigations of different heat sinks geometries have been studied.

To push the limitations of the air cooling, various heat sink structures, materials, and flow configurations have been tested. Heat sinks combine many fundamental advantages such as high convective heat transfer coefficients, large fin area in a compact layout, low pressure drop, and ease of fabrication. Goldberg [34] constructed three different mini-channels with convoluted fins for air cooling of high power semiconductors. The experimental results showed that the smallest thermal resistance occurred at the largest friction factor and smallest channel width. Also, Reynolds number and fin height were significant parameters to enhance the heat transfer rate. Lee et al [73] studied the heat transfer from heat sinks that were placed on a rectangular channel. The effect of the clearance between the tip and the shroud on the heat transfer coefficient was tested. The result showed that there was an inversely proportional relationship between the heat transfer coefficient and the clearance. Moreover, the thermal performance can be possibly enhanced by decreasing the width or increasing the height of the fins. Yokono et al. [52] studied experimentally the cooling performance of short fins (height  $\leq 5 \text{ mm}$ ) on forced

and natural air convection. The effect of fin pitch, fin height, air velocity, and heat power was tested. The study declared that the rate of heat transfer was proportional to the fin height and the air velocity. Mansuria et al. [35] performed numerical and experimental studies of three fin geometries (plate, pin, and radial) for impingement and suction flow. Impingement cooling generates lower thermal resistance than suction through the fins. The numerical simulation of 12 geometries (4 each of pin, plane, and radial fins) showed that the plate fin geometry had the minimum convection thermal resistance. For the plate fin geometry, there was a significant increase in the pressure drop when the number of fins increased. Sathyamurthy et al. [36] evaluated the performance of an inline and staggered parallel-plate heat sinks that used in the power generation systems. Three different power 100, 150, and 200 W and three different velocities 200, 400, and 600 ft. /min were used for this study. The numerical results showed a good agreement with experiment results. This study concluded that the heat transfer enhancement of the staggered fin shape was better than the planar fin shape; however, the pressure drop was more in the staggered case than in the planar case. Teertstra et al. [37] developed an analytical model to predict the average heat transfer rate for a forced air convection parallel plate heat sinks in a developed and fully developed cases. A suitable agreement was found between the model and the experimental results within error of 2.1%.

El-Sayed et al. [38] examined longitudinal rectangular fin heat sinks for parallel, impinging, and reverse impinging flows. The aim of this study was to obtain the optimal

position for the plate fin heat sink in the flow field. The working fluid was air and the flow was turbulent at Reynolds number ranging from  $7 \times 10^4$  to  $5 \times 10^5$ . The results showed that the highest heat transfer rate and lowest pressure drop were found on the parallel flow orientation. Deans et al. [53] used a new method of analyzing and designing large heat sinks. This approach was based on the effectiveness methods used to design cross-flow heat exchangers. The implementation of this approach to the design of a heat sink required the definition of a new design concept, namely, the equivalent heat capacity of the heat sink's fins. In using this approach, the heat sink was treated as one-stream heat exchanger. The predicted values for the thermal resistance of the heat sinks were found to be within  $\pm 15\%$  of the measured values. The results predicted by the new effectiveness-based design procedure generally agreed with the fin analysis approach. Didarul et al. [24] performed an experimental investigation on finned surfaces heat transfer coefficients and fluid flow characteristics in rectangular ducts with short rectangular plate fins. The working fluid was air at Reynolds number ranging from 6250 to 25,000. The variation effects of inclination angle, fin pattern, and fin height were examined. They found that the friction factors for both patterns were larger compared with the skin friction on the smooth surface for a fully developed turbulent flow. Kim et al. [39] revealed that the effective heat sink type could be determined depending on the pumping power and heat sink length by comparing the thermal performances of two types of heat sinks that are most commonly used in industry sector: plate-fin and pin-fin heat sinks. The study concluded that the thermal resistance of the optimized plate fin heat sink is low when the pumping power is small and the heat sink

length is large. However, the optimized pin fin heat sink has a low thermal resistance when the pumping power is large and the heat sink length is small.

Under cross air flow cooling, Li and Chao [40] studied experimentally the effect of Reynolds number, fin width, and fin height on the thermal performance and pressure drop of plate-fin heat sinks. As a result, an inversely proportional relationship between Reynolds number and the thermal resistance of the heat sink was found. At a constant fin width, the best thermal performance occurred with the highest fin. However, to decrease the thermal resistance, fin width must be varied as Reynolds number increases. Wu et al. [54] developed practical model to predict the hydraulic and thermal performance of a plate-fin heat sink. The model was valid for a different Reynolds numbers (laminar, transition, and turbulent flows). The accuracy of the prediction of the pressure drop was within 13.87% - 8.4% and for transitional flow ( $2000 < Re < 4000$ ), the heat transfer was predicted within error of 14% - 12%. The best values of base thickness, base length, base width, fin spacing, and fin thickness were obtained when pressure drop and fin height were set at certain values.

Prompting wall turbulence and secondary flow by inserting some roughness to the surface is one of the most common passive techniques that are used in the industry for further enhancement of the heat transfer rate. Many studies showed that the use of repeated ribs as an artificial roughness to the surface can possibly enhance the overall thermal performance of a system at a reduced pumping power [56, 69-72]. Researchers are focusing on

optimizing the geometrical parameters of rib roughness (i.e. roughness pitch, height, shape, position, etc). For the purpose of designing a turbine blade cooling channels, Han et al. [20, 21] conducted an experiment to study a fully developed turbulent air flow in square ducts with ribs on two opposite walls. The effects of the rib height to hydraulic diameter and rib pitch to height ratios on the heat transfer coefficient and friction factor were considered. Reynolds numbers were varied from 7000 to 90,000. The important highlights from the rectangular ducts with two smooth and two ribbed walls was that the Stanton number of the ribbed side wall is about 1.5 to 2.2 times the four-sided smooth duct. In addition, the Stanton number of the smooth wall is augmented by 25% since it is adjacent to ribbed wall. The average friction factor is about 2.1 to 6 times that of the four-sided smooth duct and because of the smooth walls influence, the values are about 30% to 45% lower than the four-sided ribbed duct. In the same experiment set up, Han et al. [21] developed a correlation that account for rib pitch and rib angle. The effects of the rib angle of attack and the channel aspect ratio were studied experimentally by Han et al. [22]. The temperature and pressure distributions in channels with ribs on the top and bottom walls were measured. Reynolds numbers were varied from 10,000 to 60,000 and the rib angles of attack were  $90^\circ$ ,  $60^\circ$ ,  $45^\circ$ , and  $30^\circ$ . Three different channels aspect ratio of 1, 2, and 4 were used in this experiment. The highest heat transfer which is associated to the highest pressure drop is found to be at angle of attack of  $60^\circ$  for the square channel and at  $90^\circ$  for the rectangular channel. The square channel had the best heat transfer performance with rib angle of attack ( $30^\circ$  and  $-45^\circ$ ) which is about 30% higher than that of angle of  $90^\circ$  for a

constant pumping power. A correlation for both heat transfer coefficient and friction factor that depend on some parameters such as rib pitch, rib angle, rib height, different Reynolds number, and channel aspect ratio were obtained. Moreover, Han et al. [23] performed an experiment to study the heat transfer and friction for fully developed flow of air in a square channel with nine different rib geometries on two opposite walls. The nine rib geometries were transverse and discrete ribs), parallel and crossed oblique discrete ribs ( $\alpha = 60^\circ$ ,  $45^\circ$ , and  $30^\circ$ ), and parallel oblique discrete ribs ( $\alpha = 45^\circ$  and  $-45^\circ$ ). The Reynolds number of this experiment ranged from 10,000 to 80,000. The results showed that the average Stanton number of the discrete ribs ( $\alpha = 90^\circ$ ) was a 10% to 15% higher than the transverse rib ( $\alpha = 90^\circ$ ), however, the angled ribs demonstrate a 10% to 20% higher average Stanton number than the discrete ribs ( $\alpha = 90^\circ$ ).

Soo et al. [55] examined the heat transfer coefficient and the pressure factor performance for a rectangular duct at varied Reynolds numbers from 10,000 to 70,000. Five different geometries of ribs were investigated on one side of the duct. The examined parameters were the rib shape geometry, the rib height to hydraulic diameter, pitch-to-height ratio, and channel width to height ratio. The study showed that the best heat transfer performance occurred at the triangular shaped geometry; however, the highest friction factor occurred at the square shaped geometry. Xiufang Gao et al. [74] investigated the effect of the inclined ribs on a duct on the flow behavior. The Reynolds number was set to 5800 and the rib angles of attack were varied from  $30^\circ$  to  $90^\circ$ . The conclusion of this study was that the

inclined ribs influence the strength and the style of the secondary flow. In addition, the mean flow velocity distribution alters along the span wise direction. When the angle of attack equals to  $45^\circ$ , the strongest secondary flow was observed. Shaeri et al. [75] numerically studied the conjugate heat transfer from an array of rectangular solid and perforated heat sinks inserted on a flat plate. Different numbers and multiple sizes of perforations were implemented. The turbulent flow was performed at Reynolds number ranging from 2000 to 5000. The numerical data were compared with a published experimental data and a decent agreement was found between them. The results revealed that the perforated fins obtained higher heat transfer rate and lesser drag than the solid fins. Two major highlights concluded on the perforated fins when Reynolds number was increased, first, the reduction in the drag ratio for and the heat transfer augmentation when compared with the solid fins. Layek [76] investigated the thermos-hydraulic of a solar air heater with chamfered ribs- groove roughness mounted on the absorber plate. The investigation showed that the effective efficiency and thermal performance of the roughened absorber was higher than that of the smooth case with the benefit of having the same pressure drop penalty. A strong parameter that influences the effective efficiency was found to be Reynolds number.

Park [11] explored numerically and experimentally two types of dimples (circular and oval) on a heat sink fin to increase the heat transfer on a rectangular channel. The flow was laminar and Reynolds number ranged from 500 to 1650. As a result, the dimples enhanced



the thermal performance from its surface without a pressure drop penalty. The comparison between the two types of dimples revealed that the oval dimple performed a higher thermal performance than the circular dimple. In a similar study, Iftikarahamad H. Patel and Borse [10] studied the heat transfer and flow characteristics over a dimpled surface. The Reynolds number range varied from 5000 to 15,000; the diameter and the depth were set to fixed values. The study reported that as Reynolds number increased, the thermal performance increased. Moreover, the staggered arrangement of the dimples showed higher Nusselt number than that of inline configuration.

Srivastav et al. [56] performed a numerical investigation on a ribbed fin to find the heat transfer and the friction factor under forced convection for different flow conditions. At different Reynolds numbers ranging from 500 to 5000 and different rib pitch to rib height ratio has been acquired for the numerical model. The comparison between the plain fin and the ribbed fin showed a significant heat transfer enhancement with the ribbed fin. Nusselt number increased and friction factor decreased as Reynolds number increased. Moreover, the thermo-hydraulic performance parameter is at maximum when rib pitch to its height ratio is 6 [58]. An optimal thermal design of plate fin heat sink was investigated numerically [41]. Ribs were installed in between two opposite channels in different sizes, orientation, numbers, and positions. The examined parameters were the effect of the ribs on the plate fin heat sink while keeping the number of fins fixed and the number of fins while inserting the ribs. The result revealed that, under the same boundary conditions, the

thermal performance of the ribbed plate fin heat sink is 1.55 times greater than plate fin heat sink. However, this augmentation decreased as the number of ribs increased. Prasad and Mullick [25] applied an artificial roughness to increase the thermal performance of a solar air heater. The effects of the transverse rib pitch and height were investigated. Circular wire ribs with small diameter showed a significant improvement in the heat transfer comparing to the smooth case [25-28]. [27] studied the effect of the roughness parameters as well as the operating parameters on heat transfer rate and friction factor on a roughened solar air heater. A comparison of the thermo-hydraulic performance between the roughened and the smooth case were obtained. The study reported that the maximum thermo-hydraulic performance occurred at the inclined ribs. The relative roughness height and Reynolds number which were associate with the best thermo-hydraulic performance was 0.023 and 14,000, respectively. V-shaped rib showed better heat transfer enhancement than the transverse and inclined rib [29, 30]. Momin et al. [29] investigated experimentally the heat transfer and the fluid flow characteristics of a rectangular duct with V-shaped ribs on the bottom. Reynolds numbers ranged from 2500 to 18,000, the relative roughness height ranged from 0.02 to 0.034, and the angle of attack was varied from 30° to 90°. The investigation reported that the V-shaped ribs with relative roughness height of 0.034 and angle of attack of 60° at Reynolds number of 17,034 increased the heat transfer coefficient with 2.3 times higher than that of the smooth case. Afterward multi V-shaped roughness geometry was tested which showed a significant increase in thermal performance. Hans et al. [30] reported the effect of multi-V-rib roughness on the thermal performance. Reynolds

number varied from 2000 to 20,000, the relative roughness pitch ranged from 6 to 12, the relative roughness height ranged from 0.019 to 0.043, and the angle of attack varied from 30° to 75°. The experimental results showed that the heat transfer rate enhanced by 5 times than that of a smooth case. Moreover, the friction factor was increased by 6 folds of that in the smooth case.

Sriromreun et al. [31] placed baffle turbulators on a rectangular channel. To obtain the optimum thermal performance, the effects of the Z-baffles pitch and height were experimentally tested for the range of Reynolds number from 4400 to 20,400. The baffle to channel height ratios and baffle pitch ratios were 0.1, 0.2, and 0.3, 1.5, 2, and 3, respectively. A numerical work was also conducted and the results were in a good agreement with the experimental results. The experimental results that the in-phase 45° Z-baffle showed better thermal performance than the out-phase 45° baffle at the same operation conditions. Promvonge et al. [32] investigated numerically the heat transfer and fluid flow characteristics in a square channel with 45° inline baffles on top and bottom walls for Reynolds number ranging from 100 to 1000. The results of the 45° inline baffle were compared with the 90° transverse baffle and the 45° staggered baffle. The study concluded that the inline and the staggered 45° baffles thermal enhancement were almost the same and higher than the smooth case. The heat transfer improvement in the 45° baffles found to be 100% to 200% higher than that for the 90° baffles. It also showed a 10% to 15% reduction in the friction losses. Mohammadi and Sabzpooshani [33] investigated the

effect of placing fins and baffles on the performance of the single pass solar air heater. The investigation showed that placing the fins and baffles rose the outlet air temperature and the efficiency comparing to the conventional solar air heater. It also concluded that the outlet temperature decreases as the mass flow rate increases. Bassiouny et al. [57] developed an analytical model to compare the effect of having a fully developed or thermally developing flow on heat transfer coefficient. The result showed that when a fully developed assumption considered for estimating heat transfer coefficient, the air temperature distribution was over predicted. However, when thermal entry length was considered, a good agreement between the measured and the predicted values was observed.

Besides fins and ribs, other passive techniques have been used to examine the effect of different techniques on the heat transfer rate such as coiled tubes [58-59], louvered strip inserts [44,61], winglet-type vortex generator [61-62], corrugated tubes [63-65], twisted tape [66-68]

### 2.3 Summary

There are tremendous amount of data regarding to the use of heat sinks on a turbulent flow for conventional channels, there are very few resources for the electric motor cooling applications. Therefore, the present work is intended to determine whether or not the use of parallel plate heat sinks with different ribs configurations performance can enhance the

thermal performance for electric motor application. A numerical technique will be employed. A parametric optimization study will be used to find the influence of different parameters on the performance of the electric motor cooling heat sinks.

## CHAPTER 3      NUMERICAL MODELING

In this chapter, a numerical study is conducted to simulate the airflow field, and heat transfer for a plate heat sink using ANSYS V.16. The steady, viscous, and 3D governing equations representing the flow and temperature field are described. In addition, sub-models and auxiliary equations are introduced. These sub-models include; the turbulence models that are commonly used in case of heat sinks. Moreover, the computational model, grid setup, and the method of describing boundary conditions are explained.

### 3.1 Governing Equations

The equations, which govern fluid flow and heat transfer of any nature, are the conservation equations of continuity, momentum, and energy. These are the fundamental laws, which form the basis of any detailed, rigorous method for predicting airflow field and temperature distribution within the heat sink. In order to make these relations complete, they must be supplemented with thermodynamic equations, a turbulence model, and prescribed boundary conditions. Specific terms appear in the equations depend on the case of interest due to different assumptions and possible simplifications.

Generally, heat sinks are always operated at very low Mach number and the temperature difference between the hot base and the cooling fluid is not very large so, the following assumptions have been made:

- The flow is incompressible, steady, turbulent, and three-dimensional;

- The thermo-physical properties are constant;
- The viscous dissipation in the energy equation is negligible;
- The effect of natural convection and radiation are negligible.

Based on these assumptions the governing equations take the following form:

### 3.1.1 Continuity Equation

The continuity equation is derived by balancing the mass flow rate for a control volume in the fluid flow. In tensor notation, the steady state continuity equation is expressed as [79],

$$\frac{\partial}{\partial x_i}(\rho u_i) = 0 \quad (3.1)$$

where  $u_i$  is the absolute velocity in the  $i^{th}$  direction,  $x_i$  is the coordinate in the  $i^{th}$  direction,  $\rho$  is the fluid density, and  $i$  a tensor indicating 1, 2, 3.

### 3.1.2 Momentum Equation

The momentum equations for turbulent flow are derived from Newton's second law of motion and can be expressed as [79]:

$$\frac{\partial(\rho u_i u_j)}{\partial x_j} = \frac{\partial}{\partial x_j} \left[ \mu_l \left( \frac{\partial u_i}{\partial x_j} + \frac{\partial u_j}{\partial x_i} \right) - \rho \overline{u_i' u_j'} \right] - \frac{\partial p}{\partial x_i} + S_u \quad (3.2)$$

where  $p$  is the pressure in ,  $\mu_l$  is the laminar dynamic viscosity, , and  $S_u$  is the source term.

The term on the left side of the Eq. 3.2 is the net momentum efflux, also referred to the convection term. The shear force or the diffusion term is presented by the first term on the

right side; the second term is pressure gradient term which represents the pressure forces, and the last term represents the source term.

In the diffusion term, the quantity  $[-\rho \overline{u_i' u_j'}]$  is the Reynolds stresses. It represents the turbulent transport of fluid across the main flow direction and it influences the flow in the same way as the increased shear stress. The turbulent stresses are assumed to be proportional to the gradient of the mean velocity and turbulence is assumed to be isotropic [79].

$$\tau_{ij} = -\rho \overline{u_i' u_j'} = \mu_t \left( \frac{\partial u_i}{\partial x_j} + \frac{\partial u_j}{\partial x_i} \right) - \frac{2}{3} \rho k \delta_{ij} \quad (3.3)$$

where  $\mu_t$  is the turbulent viscosity (kg/m s),  $k$  is the turbulent kinetic energy (m<sup>2</sup>/s<sup>2</sup>), and  $\delta_{ij}$  is the Kronecker delta which equals to 1 for  $i=j$  and 0 for  $i \neq j$ . In the real fluid flow the effective viscosity,  $\mu_{eff}$  can be formed as the summation of the laminar and the turbulent viscosity as:

$$\mu_{eff} = \mu_l + \mu_t \quad (3.4)$$

### 3.1.3 Energy Equation

The energy equation describes the temperature distribution throughout the non-isothermal flow domain. The derivation of this equation is from the first law of thermodynamics to the elemental control volume, and can be expressed as [79]:



$$\frac{\partial(\rho C_p u_j T)}{\partial x_j} = \frac{\partial}{\partial x_j} \left( k_{eff} \left( \frac{\partial T}{\partial x_j} \right) \right) + S_T \quad (3.5)$$

where  $C_p$  is the specific heat at constant pressure,  $S_T$  is the source term, and  $k_{eff}$  is the effective thermal conductivity which can be expressed as,

$$k_{eff} = k_l + k_t \quad (3.6)$$

where  $k_l$  is the laminar thermal conductivity and  $k_t$  is the turbulent thermal conductivity which is dependent of the local flow field.

#### 3.1.4 Auxiliary Equations

The air viscosity is computed according to the Sutherland viscosity law [77]. Sutherland's law is expressed as follows:

$$\mu = \mu_o \left( \frac{T}{T_o} \right)^{3/2} \frac{T_o + S}{T + S} \quad (3.7)$$

For air at moderate temperatures and pressures,  $\mu_o = 1.7894 \times 10^{-4} \text{Pa}\cdot\text{s}$ ,  $T_o = 273.11 \text{ K}$ , and  $S = 110.56 \text{ K}$ .

#### 3.1.5 General Form of Equations

It is possible to write above equations in a more general form for facilitating the discretization and the solution of these equations. If the dependent variable  $\phi$ , a diffusion coefficient  $\Gamma$ , and a source term  $S_\phi$  are used as general variables, the following form of the differential equations can be written as [78]:

$$\frac{\partial(\rho u_i \phi)}{\partial x_i} = \frac{\partial}{\partial x_i} \left( \Gamma_\phi \frac{\partial \phi}{\partial x_i} \right) + S_\phi \quad (3.8)$$

The left side is the convection term, the first term on the right side is the diffusion term, and the last term is the source term. All variables are summarized in Table 3.1.

### 3.2 Turbulence Models

The successful use of the above equations for real flow problems needs additional complementary relations. These additional complementary relations are turbulence models which can be used to determine the unknown variable  $\mu_t$ . The standard k- $\epsilon$  model, the RNG k- $\epsilon$ , and the standard k- $\omega$  are the most widely turbulence models that are used to simulate the airflow. These models will be discussed in the next section.

#### 3.2.1 Standard k- $\epsilon$ Model

It should be noted here that there are two major restrictions on using the k- $\epsilon$  turbulence model and these are:

- The constants used in the standard k- $\epsilon$  turbulence model need to be evaluated by experimental means which limits the general usage of the model as shown in Table 3.2.
- The standard k- $\epsilon$  model calculates the turbulent viscosity ( $\mu_t$ ) from the following relations:

$$\mu_t = C_\mu \rho \frac{k^2}{\epsilon} \quad (3.9)$$

and,

$$\varepsilon = C_D \frac{k^{\frac{3}{2}}}{L} \quad (3.10)$$

Where  $\varepsilon$  is the rate of dissipation of turbulent kinetic energy,  $C_\mu$  and  $C_D$  are empirically determined constant and  $L$  is length scale of turbulence. The calculation of turbulent viscosity thus requires derivation of two additional differential transport equations to determine  $k$  and  $\varepsilon$ . The standard k- $\varepsilon$  model therefore is called a two-equation model.

The turbulent kinetic energy can be calculated from the equation:

$$\frac{\partial}{\partial x_i} (\rho u_i k) = \frac{\partial}{\partial x_i} \left( \Gamma_k \frac{\partial k}{\partial x_i} \right) + \rho (S_k + S_B) - C_D \rho \varepsilon \quad (3.11)$$

and the turbulent kinetic energy dissipation rate can be calculated from the equation:

$$\frac{\partial}{\partial x_i} (\rho u_i \varepsilon) = \frac{\partial}{\partial x_i} \left( \Gamma_\varepsilon \frac{\partial \varepsilon}{\partial x_i} \right) + C_{\varepsilon 1} \rho \frac{\varepsilon}{k} (S_k + S_B) - C_{\varepsilon 2} \rho \frac{\varepsilon^2}{k} \quad (3.12)$$

The left hand side of Eq. 3.12 represents the convection of the dissipation of turbulent kinetic energy. On the right hand side, the 1<sup>st</sup> term is the diffusion of the dissipation of turbulent kinetic energy, and the remainder terms represent the generation destruction of the dissipation of turbulent kinetic energy.

The definition of the other terms in Eqs. 3.11 and 3.12 can be expressed as [79]:

The source term for turbulent kinetic energy:

$$S_k = \frac{\mu_t}{\rho} \frac{\partial u_i}{\partial x_j} \left( \frac{\partial u_i}{\partial x_j} + \frac{\partial u_j}{\partial x_i} \right) \quad (3.13)$$

The diffusion coefficient for turbulent kinetic energy:

$$\Gamma_k = \mu + \frac{\mu_t}{\sigma_k} \quad (3.14)$$

The diffusion coefficient for the dissipation of turbulent kinetic energy:

$$\Gamma_\varepsilon = \mu + \frac{\mu_t}{\sigma_\varepsilon} \quad (3.15)$$

Empirical constants  $C_\mu$ ,  $C_{\varepsilon 1}$ ,  $C_{\varepsilon 2}$ ,  $C_D$ ,  $\sigma_k$ ,  $\sigma_\varepsilon$  and  $\sigma_t$  given in the previous equation are discussed in the following subsections;

### 3.2.2 Empirical Constants Used in the k- $\varepsilon$ Model

Although no one set of empirical constants can be applied to every type of flow situation, there does exist an accord that a particular group of these empirical constants may be applied to a relatively wide range of problems without the need of varying any of the parameters in this group. Thus, a sacrifice of some accuracy is tolerated in view of a sense of generality in the empirical constants. The contrariwise approach to this would be to modify the collection of empirical constants for every different situation through empirical analysis and thus, resulting with nothing more than an elaborate empirical approach. The turbulent kinetic energy and corresponding dissipation equation turbulence model are assigned experimental constants [78] as listed in Table 3.2.

Table 3.1: Diffusion coefficient and source terms for variable  $\Phi$  [79].

Equation	Dependent variable ( $\phi$ )	Diffusion Coefficient ( $\Gamma_\phi$ )	Source term ( $S_\phi$ )
Continuity	1	0	0
x- Momentum	U	$\mu + \mu_t$	$-\frac{\partial P}{\partial x} + \frac{\partial}{\partial x} \left( \mu_t \frac{\partial U}{\partial x} - \frac{2}{3} \rho \cdot k \right) + \frac{\partial}{\partial y} \left( \mu_t \frac{\partial V}{\partial x} \right) + \frac{\partial}{\partial z} \left( \mu_t \frac{\partial W}{\partial x} \right)$
y- Momentum	V	$\mu + \mu_t$	$-\frac{\partial P}{\partial y} + \frac{\partial}{\partial x} \left( \mu_t \frac{\partial U}{\partial y} - \frac{2}{3} \rho \cdot k \right) + \frac{\partial}{\partial y} \left( \mu_t \frac{\partial V}{\partial y} \right) + \frac{\partial}{\partial z} \left( \mu_t \frac{\partial W}{\partial y} \right)$
z- Momentum	W	$\mu + \mu_t$	$-\frac{\partial P}{\partial z} + \frac{\partial}{\partial x} \left( \mu_t \frac{\partial U}{\partial z} - \frac{2}{3} \rho k \right) + \frac{\partial}{\partial y} \left( \mu_t \frac{\partial V}{\partial z} \right) + \frac{\partial}{\partial z} \left( \mu_t \frac{\partial W}{\partial z} \right)$
Temperature	T	$\mu + \frac{\mu_t}{\sigma_t}$	0
Turbulent kinetic energy	k	$\mu + \frac{\mu_t}{\sigma_k}$	$\rho(S_k + S_B) - \rho \epsilon C_D$
Dissipation rate	$\epsilon$	$\mu + \frac{\mu_t}{\sigma_\epsilon}$	$C_{1\rho} \frac{\epsilon}{k} (S_k + S_B) - C_{2\rho} \frac{\epsilon^2}{k}$

Most of turbulence models are based on the concept that the turbulent stresses are proportional to the mean velocity gradients, analogous to the viscous stresses in laminar flow.

Table 3.2: Empirical constants used in the k- $\epsilon$  model [78].

$C_\mu$	$C_{\epsilon 1}$	$C_{\epsilon 2}$	$C_D$	$\sigma_k$	$\sigma_\epsilon$	$\sigma_t$	$\sigma_c$
0.09	1.44	1.92	1.0	1.0	1.3	0.85	0.7

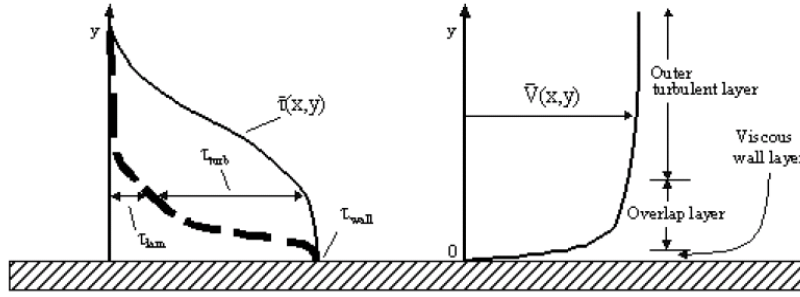
### 3.3 Near-Wall Treatment for Turbulent Flows

A strong velocity gradient and an essential viscosity effects occurred near the walls.

Due to the viscous damping near the wall, the tangential velocity fluctuations decreases and kinematic blocking reduces the normal fluctuations. At the outer portion of near wall region, Reynolds stress and large gradient of the mean velocity produce turbulent kinetic energy which therefore augment the turbulence. Figure 3.1 shows the velocity and shear distributions in turbulent flow near the wall [78].

Many experiments showed that the near wall region can be subdivided into three layers which namely as:

- Innermost layer termed the viscous sub-layer, where the flow is almost laminar like. Viscosity plays a major rule in heat transfer and momentum.
- Outer layer termed the fully turbulent layer in which the turbulence plays the key rule. This layer is far away from the wall, therefore, velocity and other variables don't depend on viscosity.
- Intermediate region between the viscous sub-layer and the fully turbulent layer termed buffer layer, where the effects of viscosity and turbulence are both significant.



(a) Shear Distribution      (b) Velocity Distribution

Figure 3.1: Typical velocity and shear distribution in turbulent flow near the wall [78]

In the near-wall region, the velocity has a common distribution as in Fig. 3.2. According to numerous measurements, the fully turbulent region and the viscous sub-layer can be represented as functions between the dimensionless wall distance  $y^+$  and dimensionless velocity  $u^+$ , [78].

$$\text{Viscous sub-layer: } u^+ = y^+ \quad 0 \leq y^+ \leq 5 \quad (3.16)$$

$$\text{Fully-turbulent region: } u^+ = \frac{1}{K_c} \ln y^+ + c^+ \quad 60 < y^+ \quad (3.17)$$

Where:

$$u^+ = \frac{u}{u_t} \quad , \quad y^+ = \frac{\rho u_t y}{\mu}$$

and;

$K_c$  : is the Von Karman constant ( $K_c = 0.4187$ ).

$c^+$  : is an empirical constant ( $c^+ = 5.45$ ).

$u_t$  : is the wall friction velocity ( $u_t = \sqrt{\tau_w / \rho}$ ).

$u$  : is the velocity parallel to the wall.

$\tau_w$  : is the wall shear stress.

$y$  : is the normal distance to the wall.

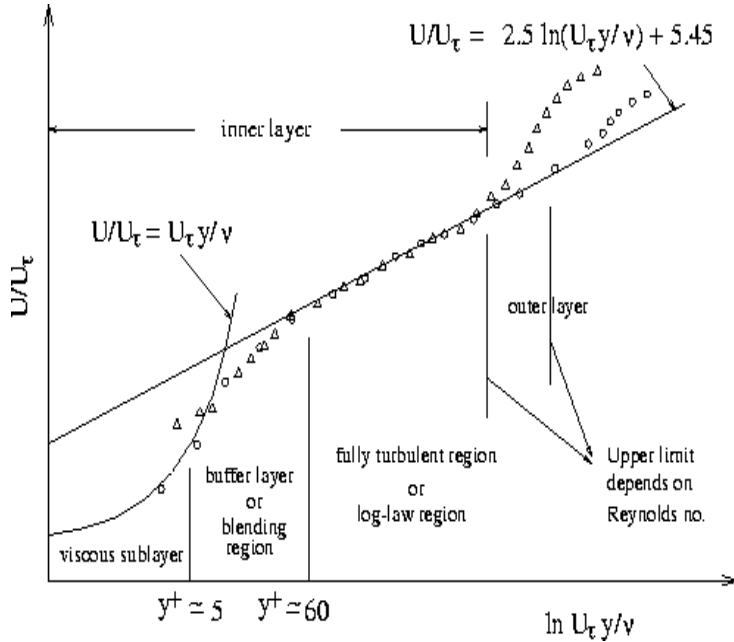
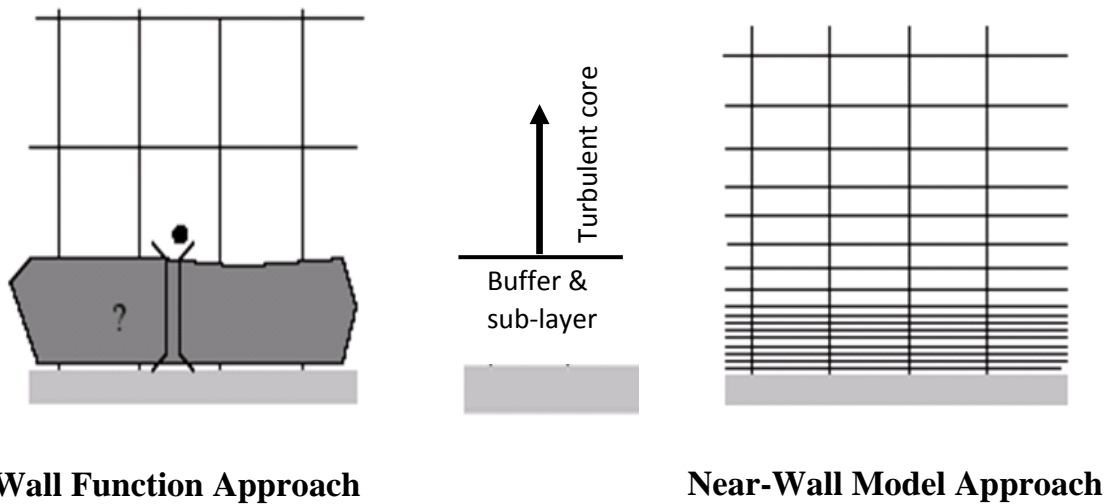


Figure 3.2: Subdivisions of the Near-Wall region [78]

Two approaches have been found for modeling the near-wall region. The first approach is the wall function approach. In this approach semi-empirical formulas are used to link the viscous sublayer and the buffer layer between the wall and the fully-turbulent region. Usage of wall functions prevent the requirement of modifying the turbulence models when considering the presence of the wall. The second approach is the near wall modeling approach or the enhanced wall treatment. In this approach, the turbulence model is modified to allow the viscosity-affected region to be resolved with a mesh all the way to the wall. The near-wall mesh must be fine enough to be able to resolve the laminar sublayer (typically  $y^+ \approx 1$ ). This demand imposes too large computational requirement.



These two approaches are shown schematically in Fig. 3.3. It is apparent that the wall functions approach is the cost effective alternative to the enhanced wall treatment and it will be used in this simulation. The standard wall function is one choice that's the FLUENT offers in the wall function approaches which has been used in this study. More details about turbulence modeling and near wall treatment can be found in FLUENT user's guides [78].



- The viscosity affected region is not resolved, instead is bridged by the wall function.
  - High Re turbulent models can be used.
- The near-wall region is resolved all the way down to the wall.
  - The turbulent models ought to be valid throughout the near-wall region.

Figure 3.3: Near-wall treatments in FLUENT [78]

### 3.3.1 The Standard Wall Function

The standard wall functions have been most widely used for industrial flows. They are provided as a default option in FLUENT mainly the momentum, energy, and species equation that is [78]:

- For Momentum

The law-of-the-wall for mean velocity yields

$$U^* = \begin{cases} y^* & y^* < 11.225 \\ \frac{1}{k_c} \ln(Ey^*) & y^* > 11.225 \end{cases} \quad (3.18)$$

where

$$U^* \equiv \frac{U_p C_\mu^{1/4} k_p^{1/2}}{\tau_w / \rho} \quad (3.19)$$

$$y^* \equiv \frac{\rho C_\mu^{1/4} k_p^{1/2} y_p}{\mu} \quad (3.20)$$

Where

$E$  : is an empirical constant ( $E = 9.793$ ).

$U_p$  : is mean velocity of the fluid at point  $P$ .

$k_p$  : is the turbulence kinetic energy at point  $P$ .

$y_p$  : is the distance from point  $P$  to the wall.

When the mesh is such that  $y^* < 11.225$  at the wall-adjacent cells, FLUENT applies the laminar stress-strain relationship that can be written as:

$$U^* = y^* \quad (3.21)$$

- For Energy

Similar logarithmic law for mean temperature has been found from Reynold's analogy between the energy and momentum transport. The law of the wall for temperature applied in FLUENT contains two different laws [78]:

- Linear law for the thermal conduction sublayer where conduction is imperative.
- Logarithmic law for the turbulent region where effects of turbulence control conduction.

There is a difference between the thermal conduction layer thickness and the viscous sublayer thickness. The law-of-the-wall executed in FLUENT has the following form:

$$T^* \equiv \frac{(T_w - T_p) \rho C_p C_\mu^{1/4} k_p^{1/2}}{q} = \begin{cases} P_r y^* + \frac{1}{2} \rho P_r \frac{C_\mu^{1/4} k_p^{1/2}}{q} U_p^2 & (y^* < y_T^*) \\ P_{rt} \left[ \frac{1}{k} \ln(E y^*) + P \right] + \frac{1}{2} \rho P_r \frac{C_\mu^{1/4} k_p^{1/2}}{q} [P_{rt} U_p^2 + (P_r - P_{rt}) U_c^2] & (y^* > y_T^*) \end{cases} \quad (3.22)$$

Where P can be calculated as [78]:

$$P = 9.24 \left[ \left( \frac{P_r}{P_{rt}} \right)^{3/4} - 1 \right] [1 + 0.28 e^{-0.007 P_r / P_{rt}}] \quad (3.23)$$

and

$k_p$  : Turbulent kinetic energy at point  $P$ .

$\rho$  : Density of fluid.

$C_p$  : Specific heat of fluid.

$q_w$  : Wall heat flux.

$T_p$  : Temperature at the cell adjacent to wall.

$T_w$  : Temperature at the wall.

$P_r$  : Prandtl number ( $\mu C_p/k_f$ ).

$P_{rt}$  : Turbulent Prandtl number (0.85 at the wall).

$U_c$  : Mean velocity magnitude at  $y^* = y_T^*$ .

Hint, for the pressure-based solver, the terms:

$$\frac{1}{2} \rho P_r \frac{C_\mu^{\frac{1}{4}} k_p^{\frac{1}{2}}}{q_w} U_p^2 \quad \text{and} \quad \frac{1}{2} \rho P_r \frac{C_\mu^{\frac{1}{4}} k_p^{\frac{1}{2}}}{q_w} [P_{rt} U_p^2 + (P_r - P_{rt}) U_c^2]$$

will be comprised in Eq. 3.22 for compressible flow calculations only.

### 3.4 Numerical Methods

An analytical solution of the coupled, nonlinear, partial differential equations for three dimensional turbulent flow field is not possible. The use of numerical methods is inevitable therefore; the solving of a CFD problem usually involves five major components: geometry, grid generation, setting-up a physical model, solving the model, and post-processing the results.

The computational domain is constructed by SolidWorks while the mesh is generated by using ANSYS Workbench 16.0. Finite volume method is used to obtain the numerical solution using Fluent 16.0.

### 3.5 Problem Description and Modeling

In order to have a complete description of the present problem numerically, steps shown in flow chart given in Fig. 3.4 should be carried out:

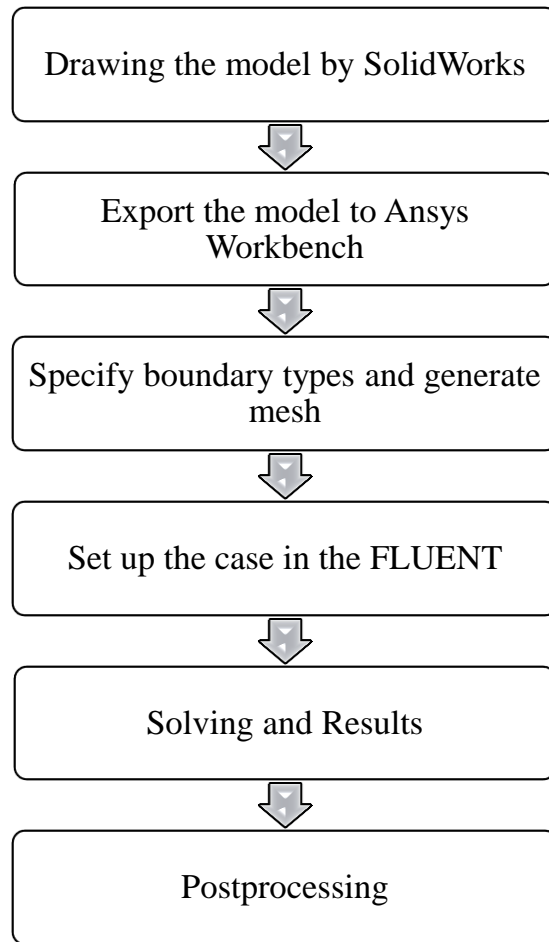


Figure 3.4: Problem set-up flow chart

#### 3.5.1 Model Description

The domain considered in the present work is a simple design of an electric motor annulus. The electric motor annulus consists of an array of ribbed fins as shown in Fig. 3.5. To simplify the simulation process, the cylindrical coordinate is changed to cartesian

coordinate since there are only three to four degree of space between each two fins. In addition, the concept of symmetry is used. A fluid domain and one half of two adjacent fins width are considered as the computational domain as shown in Fig. 3.6. The domain looks like a rectangular channel of  $L_{ch} \times W_{ch} \times H$ . The solid plate fin has thickness of (a) and is attached to a solid rectangular base that has thickness (b). Heat source is represented as a uniform heat flux at the bottom surface of the heat sink base. Through the simulations, the rib height (e) and spacing (p) between the ribs, the channel width, and the rib configuration are varied to study their effect on the performance of the heat sink. The dimensions of the computational domain and the parameters that using through the simulation are coming from a typical commercial electric motor as shown in Table 3.3.

Figure 3.6 (b), demonstrates an inline ribs configuration which has the same parameters as the continuous ribs in Fig. 3.6 (a) except that the channel width is changed to 6 mm. For the inline ribs, different number of openings with 0.5 mm height are investigated and the opening ratio is calculated as follows:

$$OR = \frac{0.5 \cdot N}{10} \times 100 = 5 N \% \quad (3.24)$$

where,  $N$  indicates the number of opening through the solid rib.



Figure 3.5: Electric motor annulus with ribbed fins

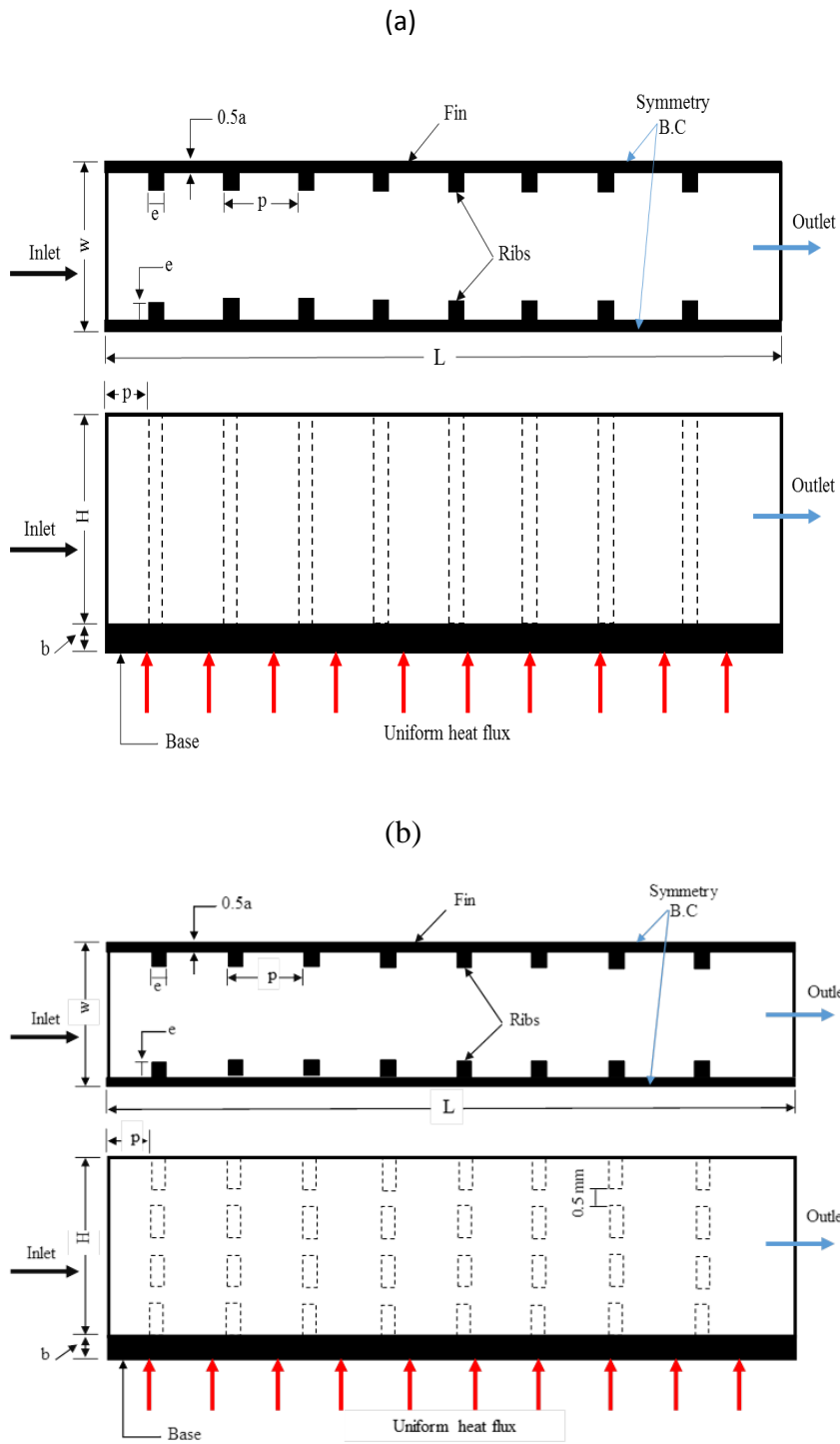


Figure 3.6: Computational domain, (a) continuous ribs configuration, (b) inline ribs configuration

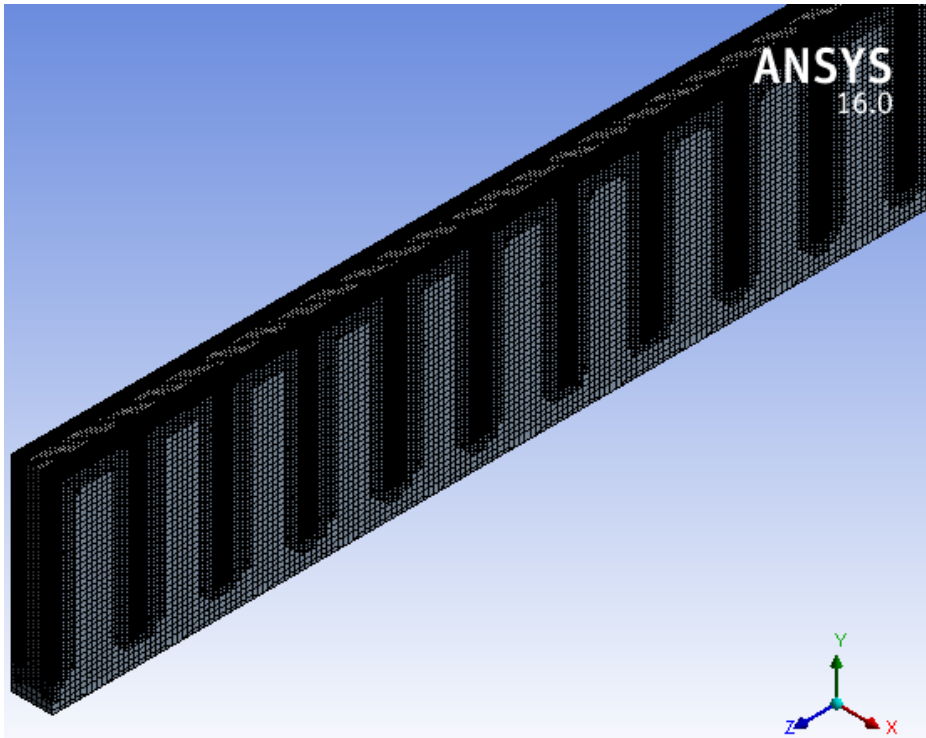


Table 3.3: Heat sink parameters

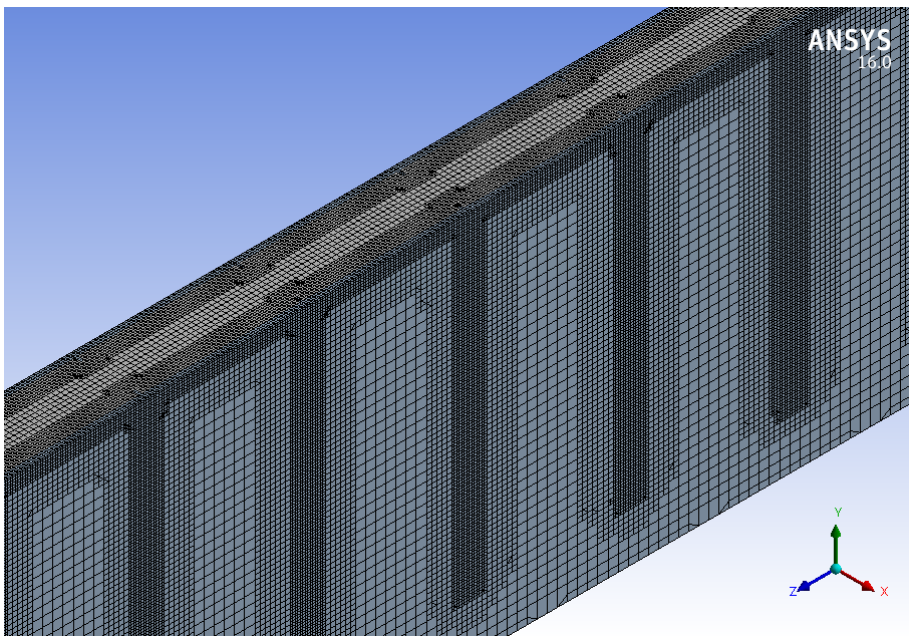
Parameter	Value [mm]
$L_{ch}$	200
$W_{ch}$	2
H	10
b	2
a	0.4
p	1, 2, 3, 4, 5
e	0.05, 0.1, 0.2

### 3.5.2 Grid Generation

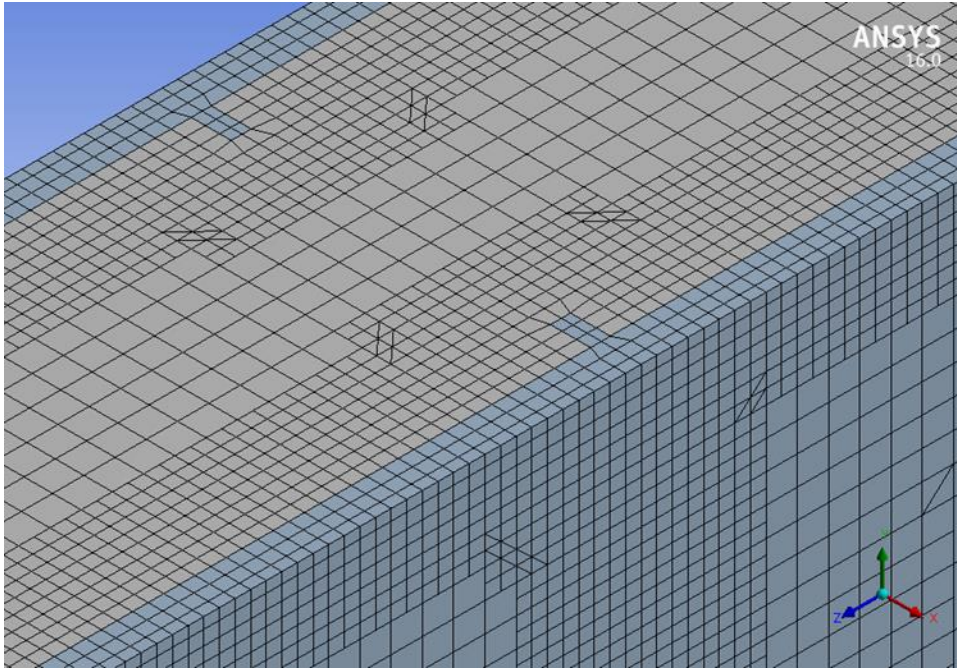
Discretization in a space requires that the flow field should be divided into small control volumes. Different types of control volumes and grid topologies are possible, including hexahedral and tetrahedral control volumes and structured or unstructured grids. Hexahedral control volumes and structured grid is used as shown in Fig. 3.7. It is clear that the mesh is very fine near the walls and around the ribs to capture the flow behavior in these areas.



(a)



(b)



(c)

Figure 3.7: Structured and hexahedral mesh for the present heat sink

### 3.5.3 Boundary Conditions

In order to solve the governing equations, boundary conditions need to be imposed on the boundaries of the numerical domain. No-slip boundary condition is used along the walls. Symmetry boundary condition is used for the mid-plane of the fin which the temperature gradient or heat transfer flux is zero. Uniform heat flux of  $12250 \text{ W/m}^2$  is used as a heat source on the bottom side of the heat sink base as shown in Fig. 3.6.

At the inlet boundary, all properties are assumed to be uniform across the section. The properties specified here include four different velocity magnitudes (15, 20, 40, and 60 m/s) and temperature of 293.15 K. Furthermore, for turbulent flows, turbulence intensity of 5% and turbulent viscosity ratio of 10 is used; moreover, hydraulic diameter must be set

at the inlet section. At the exit boundary, atmospheric pressure is considered. Initial conditions are required throughout the domain to start the solution.

### 3.6 Solver and calculations

The code "ANSYS Fluent V 16.0" is used in this study. A control-volume-based technique is used to transform the governing equations to algebraic equations which can be solved numerically. In this technique, the governing equations are integrated at each control volume. The Pressure-Based solver is selected to solve the airflow field in “Fluent” software. The Semi-Implicit Method for Pressure-Linked Equations (SIMPLE) used as the numerical algorithm in the pressure-velocity coupling which uses a combination of continuity and momentum equations to derive an equation for pressure (or pressure correction).

Flow and temperature field are solved numerically. Temperature profile over the heater is used to calculate the local and average Nusselt number of the heat sink at different Reynolds numbers where Reynolds number is calculated based on hydraulic diameter as:

$$Re_{D_h} = \frac{\rho \cdot u \cdot D_h}{\mu} \quad (3.25)$$

where  $\mu$  represents the fluid viscosity in Pa.s,  $D_h$  is the hydraulic diameter and it is calculated as,

$$D_h = \frac{4 \cdot A_c}{P} \quad (3.26)$$

The local heat transfer coefficient and local Nusselt number based on the hydraulic diameter are calculated as,

$$h = \frac{q}{T_w - T_i} \quad (3.27)$$

$$Nu = \frac{h D_h}{k_f} \quad (3.28)$$

while the average Nusselt number and heat flux are calculated as following,

$$\overline{Nu} = \frac{1}{L_{ch}} \int_0^{L_{ch}} Nu \, dx \quad (3.29)$$

$$q = \frac{Q}{A} = \frac{Q}{\tau \cdot D_m \cdot L_{ch}} = \frac{1000W}{\tau \cdot 0.13m \cdot 0.2m} = 12250 \, W/m^2 \quad (3.30)$$

where  $L_{ch}$  is the channel length,  $k_f$  is the fluid (air) thermal conductivity,  $T_w$  is the wall temperature,  $T_i$  is the inlet temperature, and  $Q$  is the motor heat input.

Friction factor is estimated as follows:

$$f = \frac{\frac{\Delta p}{L} D_h}{\frac{1}{2} \rho v^2} \quad (3.31)$$

where  $\Delta P$  is the pressure drop,  $\rho$  is the fluid density,  $v$  is the fluid velocity.

Accordingly, to evaluate the heat transfer performance considering the pressure drop penalty at the same pumping power and to see whether adding ribs to the channel enhances the thermal-hydraulic performance or not a thermal-hydraulic performance

evaluation factor ( $JF$ ) is used. This factor can be derived and calculated from the following equations:

$$PP = \Delta P * \dot{V} \quad (3.32)$$

Divide and multiply the right hand side by  $\frac{1}{2} \rho v^2$  to get the following:

$$PP = \frac{\Delta P}{\frac{1}{2} \rho v^2 \frac{L}{D}} * \frac{1}{2} \rho v^2 \frac{L}{D} * (A * v) \quad (3.33)$$

$$PP = f * \frac{1}{2} \rho v^3 \frac{L}{D} * A * \frac{\rho^2 D^3}{\mu^3} * \frac{\mu^3}{\rho^2 D^3} \quad (3.34)$$

$$PP = f * Re^3 * \frac{1}{2} \frac{L}{D^4} * A * \mu^3 \quad (3.35)$$

Now compare the ribbed fin case to the fully developed smooth case at the same pumping power:

$$PP_r = PP_{s,fd} \quad (3.36)$$

$$(f * Re^3 * \frac{1}{2} \frac{L}{D^4} * A * \mu^3)_r = (f * Re^3 * \frac{1}{2} \frac{L}{D^4} * A * \mu^3)_{s,fd} \quad (3.37)$$

The term of  $\frac{1}{2} \frac{L}{D^4} * A * \mu^3$  is constant in both cases, therefore, it will cancel each other to get:

$$(f * Re^3)_r = (f * Re^3)_{s,fd} \quad (3.38)$$

$$(f_r * Re^3)_r = (f_{s,fd} * Re^3)_{s,fd} \quad (3.39)$$

$$[Re^3]_{s,fd}^{\frac{1}{3}} = \frac{f_r}{[f_{s,fd}]} * [Re^3]^{\frac{1}{3}} \quad (3.40)$$

$$(Re)_{s,fd} = \left[ \frac{f_r}{f_{s,fd}} \right]^{\frac{1}{3}} * (Re)_r \quad (3.41)$$

$$JF = \left( \frac{\bar{h}}{h_{s,fd}} \right)_{pp} = \left( \frac{\overline{Nu}}{Nu_{s,fd}} \right)_{pp} \quad (3.42)$$

Then the thermal-hydraulic performance factor is calculated from the following equation:

$$JF = \frac{\frac{\overline{Nu}_r}{Nu_{s,fd}}}{\left( \frac{\bar{f}_r}{f_{s,fd}} \right)^{\frac{1}{3}}} \quad (3.43)$$

here,  $Nu_{s,fd}$  and  $f_{s,fd}$  represent the smooth fully developed Nusselt number and friction factor, respectively.  $PP$  is the pumping power and  $\dot{V}$  is the volumetric flow rate.

### 3.7 Gird Sensitivity

Several structured grids are performed with different mesh sizes in order to guarantee the grid independence of the results. Fig. 3.8 shows the average Nusselt number and friction factor at different mesh sizes for heat sink with pitch size of 5 mm and rib height of 0.2 mm. In this graph, the obtained results from meshes size of more than 3.5 million are similar. So, the results from 4 million grid size can be considered as grid independent solution.

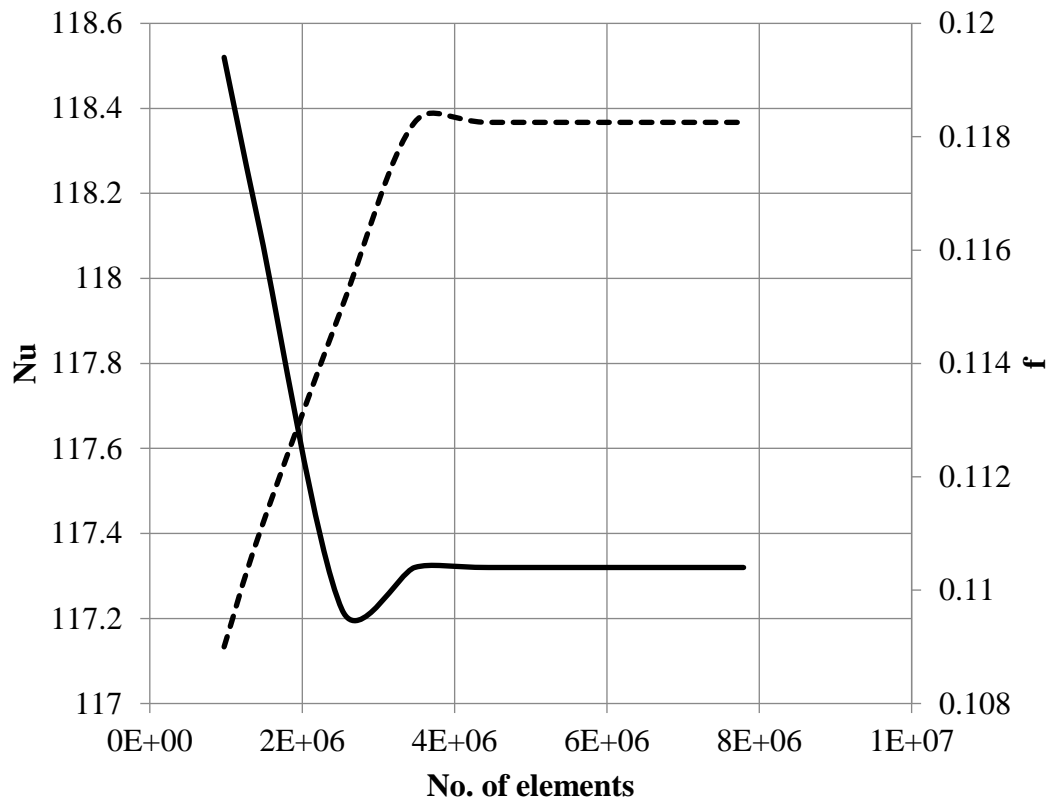


Figure 3.8: Variation of Nusselt number with the number of mesh elements.

### 3.8 Code Validation

A detailed investigations described in this section is undertaken to validate the numerical code (FLUENT 16.0) for the present application. The accuracy of the predicted results is established through the validation technique. Experimental available results from a previous work [22] is used to validate the present code.

Three different cases are performed where the geometries differ from one to another. However, the dimensions of the geometry of the rectangular channel are 10.2, 2.5, and 127.4 cm for width, height, and length, respectively. Moreover, the rectangular channel has



periodic ribs which are placed on the top and bottom of the channel width side. The rib geometries on the test channel are 0.32 cm for both height of the rib from the surface and the thickness, the rib pitch is 3.2 cm, and rib angles of attack are  $30^\circ$  and  $90^\circ$ . In addition, Reynold's number is calculated based on the channel hydraulic diameter (0.0408 m) which is 30,000. The channel is heated from all faces with a uniform heat flux of  $950 \text{ W/m}^2$  and the entrance air velocity is 11.5 m/s. For the purpose of validation, a rectangular channel with periodic ribs placed on the top and bottom of the channel width side is modeled and same boundary conditions are applied as shown in Fig. 3.9.

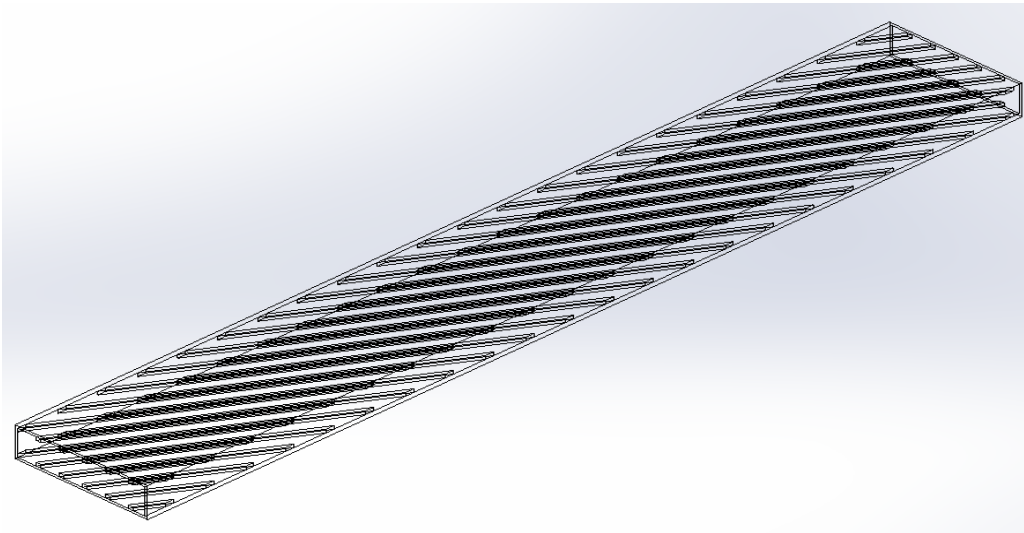


Figure 3.9: The ribbed channel model with a rib angle of  $30^\circ$

The validity established by comparing Nusselt Number and the friction factor from [22] with the numerical models simulation using ( ANSYS FLUENT 16.0) which uses the Finite Volume Method (FVM). The present validity work first started with specifying the problem parameters. After that the models were built using Solid Works and after that

imported to the Model Builder on ANSYS. Next, mesh was generated by using three different turbulent models (standard k- $\epsilon$ , RNG k- $\epsilon$  and SST k- $\omega$ ) and three different numbers of mesh elements (one, three and four millions). The purpose of this is to assure that the solution is mesh independent. All the turbulent models and the numbers of mesh elements showed similar solutions. Therefore, the standard k- $\epsilon$  and the one million elements were chosen for the validity since this will take less time than three or four millions numbers of mesh elements.

The calculation of the local heat transfer coefficient was the same way as in [22]. Given the heat flux and from the simulation result wall temperature and mean temperature can be found, therefore, heat transfer coefficient calculated as in Eq.3.27, and the local Nusselt number can be calculated as in Eq.3.28. The friction factor found by using Eq. 3.31

For the smooth fully developed circular ducts, the following correlation is used during the validation process [78]

$$Nu_{s,fd} = 0.023 Re^{0.8} Pr^{0.4} \quad (3.44)$$

While the friction factor is normalized by the friction factor for fully developed turbulent flow ( $10^4 < Re < 10^6$ ) proposed by Blasius [78],

$$f_{s,fd} = 0.046 Re^{-0.2} \quad (3.45)$$

Figure 3.10 shows a comparison between the present numerical simulation and [22] experiment ( $\theta = 30^\circ$ ) results. It shows a good agreement between the two ways. As a result, the present code can be used to simulate and study the hydrodynamic and thermal performance of a plate heat sink with ribs used for the electric motor cooling. Therefore, same comparison applied for the ( $\theta = 90^\circ$ ) case and it showed a good agreement as well and the results are shown on Table 3.4.

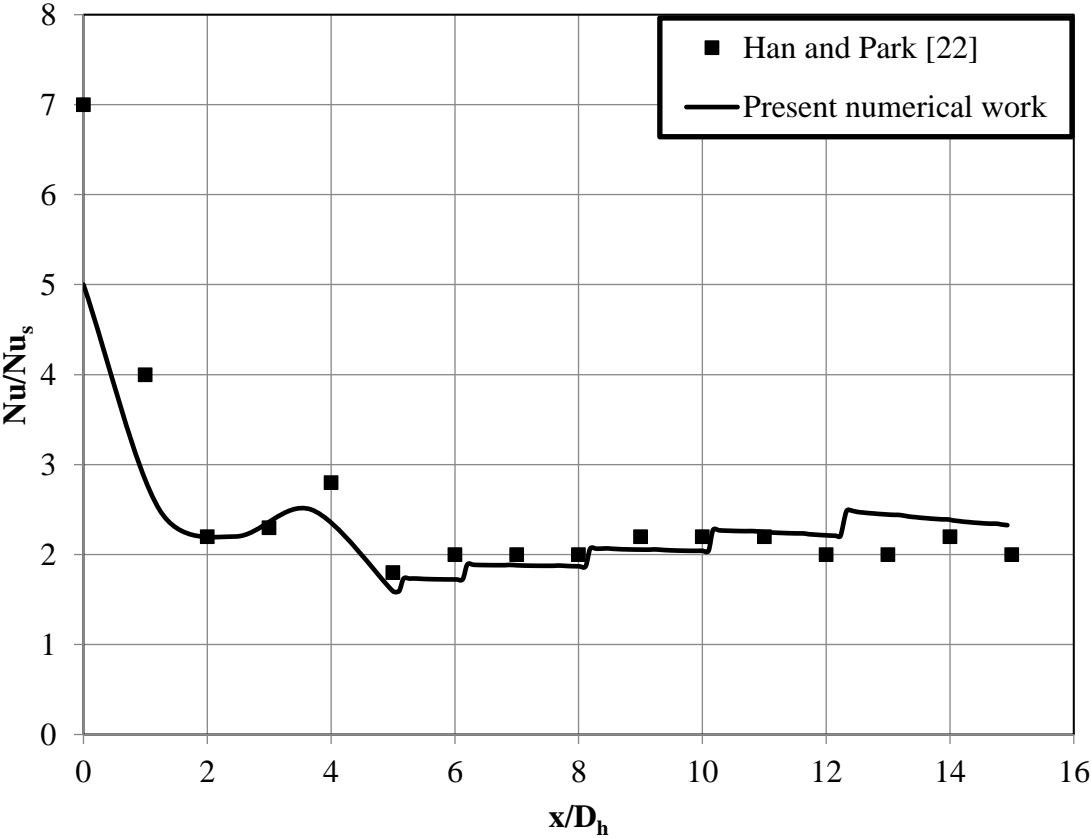


Figure 3.10: Comparison of the Numerical results with [22] experimental results.

The following table 3.4 demonstrates the comparison between the experimental results [77] and the numerical results. The comparison shows a good agreement between the

previous and present results for both cases of 30° and 90° angle of attack. All the three ratios  $\frac{\overline{Nu_r}}{Nu_{s,fd}}$ ,  $\frac{\overline{f_r}}{f_{s,fd}}$ , and  $JF$  show an error percentage of less than 5% which is really decent.

Table 3.4: Comparison between the present numerical results and the experimental results [22].

	$\theta$	<b>Present numerical results</b>	<b>Experimental results</b>	<b>% Deviation</b>
$\frac{\overline{Nu_r}}{Nu_{s,fd}}$	30°	2.17	2.2	1.36%
	90°	2.88	2.75	4.7%
$\frac{\overline{f_r}}{f_{s,fd}}$	30°	6.1	6	1.63%
	90°	15.91	16	0.56%
$JF$	30°	1.19	1.21	1.65%
	90°	1.14	1.10	3.5%

## CHAPTER 4 RESULTS AND DISCUSSION

In this chapter, the flow field and heat transfer are simulated at various design parameters of the heat sink. The numerical results are focused on showing the main parameters that define the heat sink performance, which are the pressure drop and heat transfer. A parametric study is performed to show the effect of Reynolds number, rib height, rib pitch, rib configuration, and rib opening ratio on the heat sink performance. Moreover, correlations relating the Nusselt number and friction factor to Reynolds number at different design parameters are obtained.

### 4.1 Base Smooth Case Performance

To discuss the effect of different design parameters on the heat sink performance, a base smooth case with specific design is considered first. Detailed descriptions of the design parameters and operating conditions of the base case is shown in Table 4.1. Friction factor ( $f$ ), Nusselt number ( $Nu$ ), and thermal-hydraulic performance factor ( $JF$ ) are used to evaluate the performance of the rib fin heat sink. Fig. 4.1 and Fig. 4.2 show the trend of the average Nusselt number and friction factor with Reynolds number, respectively. There is a proportional relationship between the average Nusselt number and Reynolds number. However, an inversely proportional relationship between friction factor and Reynolds number is shown in Fig. 4.2.

Table 4.1: Values of the Parameters Considered in the Base Smooth Case

Parameter	Value	
Air Inlet Temperature	20 °C	
Heat Input	1000 W	
Reynolds Number Range	3133 to 12532	
Heat sink Dimension	Fin Height, H	10 mm
	Fin Thickness, a	0.4 mm
	Channel width, $W_{ch}$	2 mm
	Length, $L_{ch}$	200 mm
	Base, b	2 mm

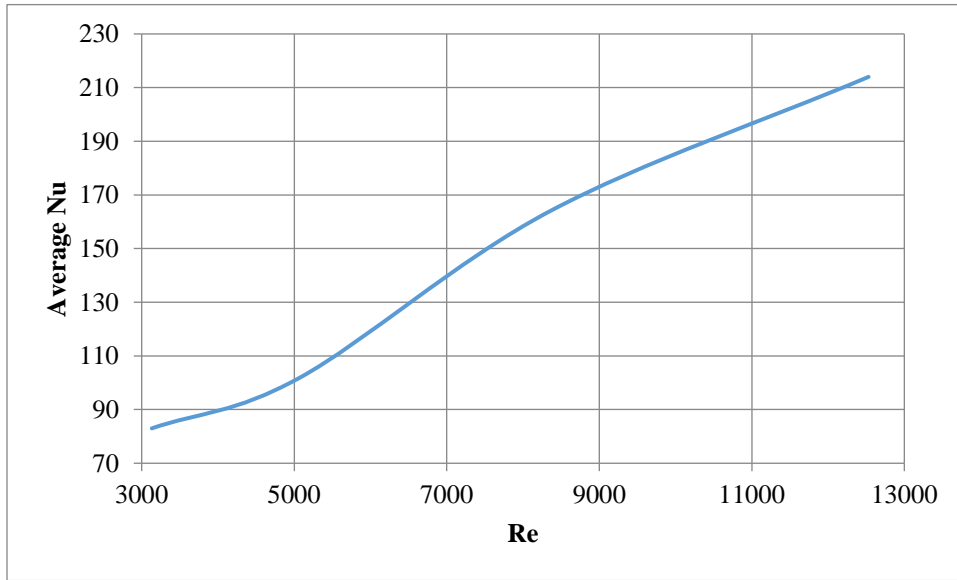


Figure 4.1: Variation of the Average Nusselt Number with Reynolds Number for the Base Smooth Case Performance

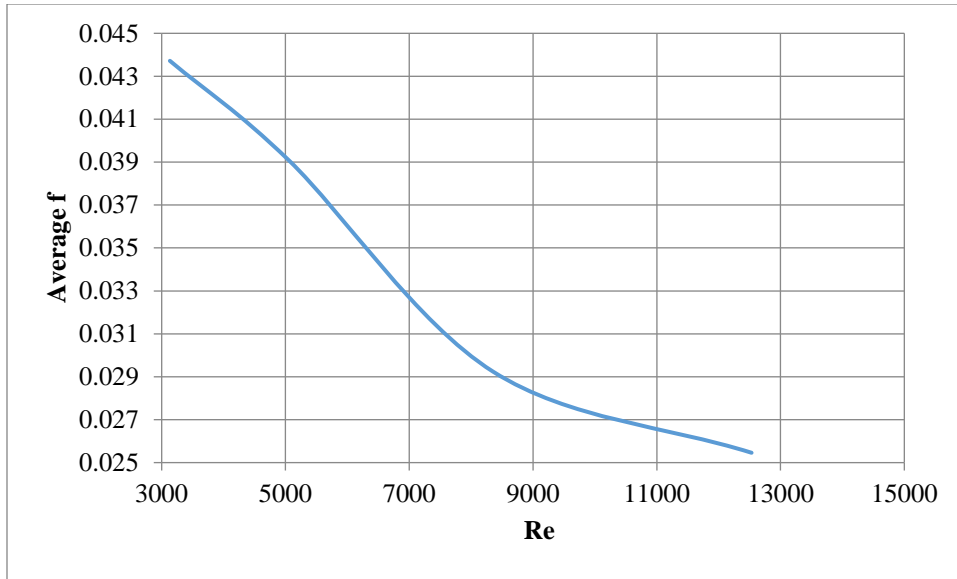


Figure 4.2: Variation of the Friction Factor with Reynolds Number for the Base Smooth Case Performance.

#### 4.2 Transverse Ribs

Continuous transverse ribs are placed on the two sides of the fin to generate a flow region on each side of the rib as shown in Fig. 3.6. The presence of ribs on a wall introduces two heat transfer enhancing features, an increase in heat transfer area and a significant increase in heat transfer coefficients. The increase in heat transfer coefficient is attributed to the effect of the ribs in disturbing/destruction of the thermal boundary layer generated on the wall. The maximum heat transfer happens to be at the region downstream from where the flow separated and reattached again as shown in Fig. 4.3. Rib pitches of 1, 2, 3, 4, and 5 mm and different rib height of 0.05, 0.1, and 0.2 mm are tested.

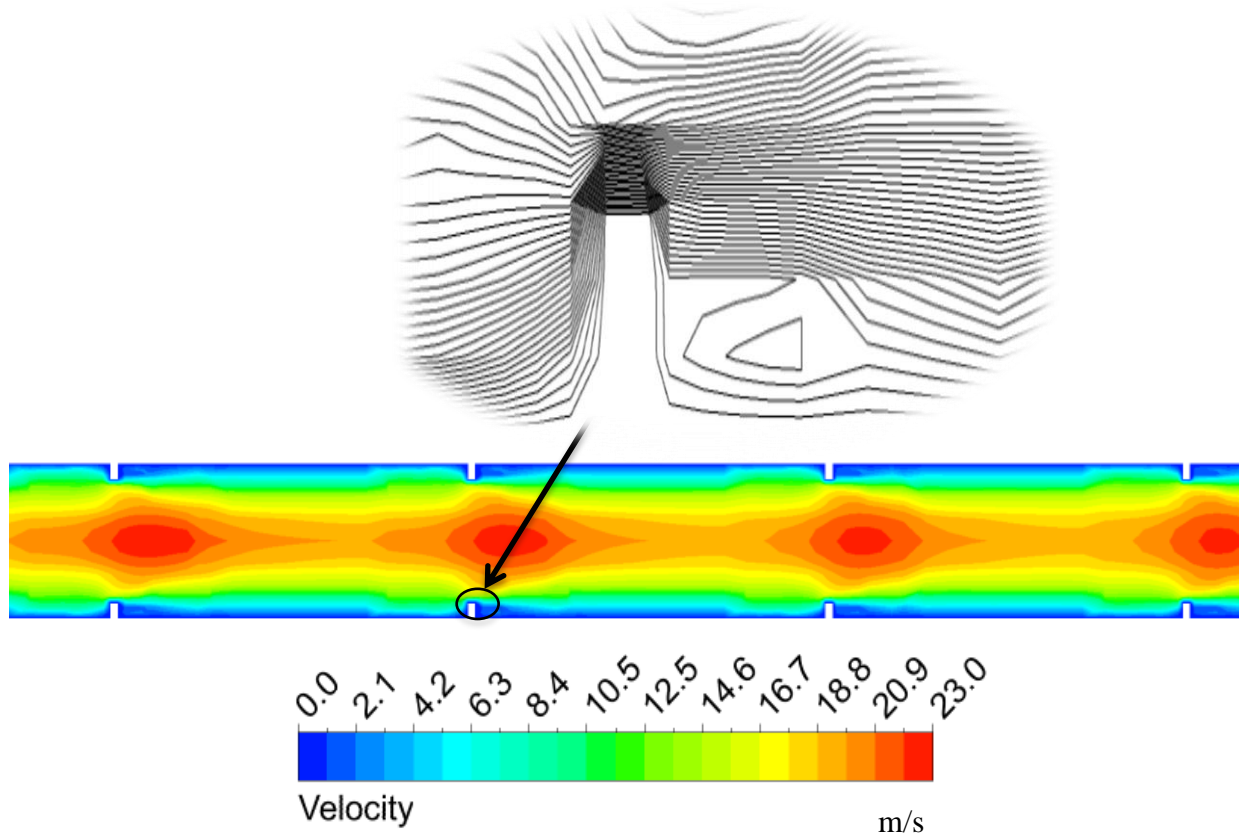


Figure 4.3 Velocity Contour over the case where  $p=5$  mm,  $e=0.2$  mm, and  $Re=3133$ .

#### 4.2.1 Effect of Rib Pitch and Height

To evaluate the heat transfer performance considering the pressure drop penalty at the same pumping power and compare it with the base case performance, Figs. 4.4 - 4.12 show the relationship of  $\overline{Nu}_r/\overline{Nu}$ ,  $\overline{f}_r/\overline{f}$ , and  $JF$  with four different Reynolds numbers. As can be seen from Figs. 4.4 - 4.9, the average Nusselt number ratio decreases as Reynolds number increases. Rib pitch of 1 mm produces the highest average Nusselt number ratio for the three rib heights. Furthermore, as the rib height increases, the average Nusselt number ratio increases. The proposed geometry of  $e=0.1$  mm,  $p=5$  mm, and  $Re=3133$  yields average Nusselt number ratio of 1.26, and 1.63 at  $e=0.2$  mm,  $p=1$  mm, and  $Re=3133$ . The friction factor is about 1.72 at  $e=0.05$  mm and  $p=5$  mm while it is around 12.4 times higher than the base smooth case at  $e=0.2$  mm and  $p=1$  mm. Unlike the average Nusselt number ratio,



friction factor ratio increases when Reynolds number increases and heat sinks of 1 mm pitch have the highest value.

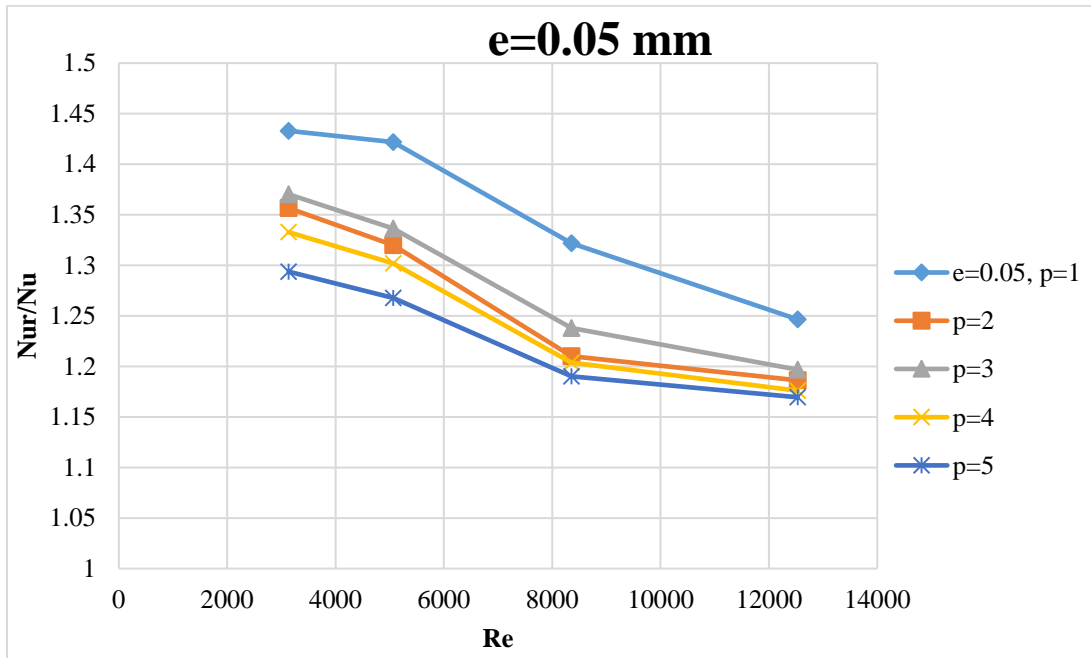


Figure 4.4: Variation of the average Nusselt number ratio with Reynolds number for a fixed value of  $e=0.05$  mm and different values of  $p$  (in mm).

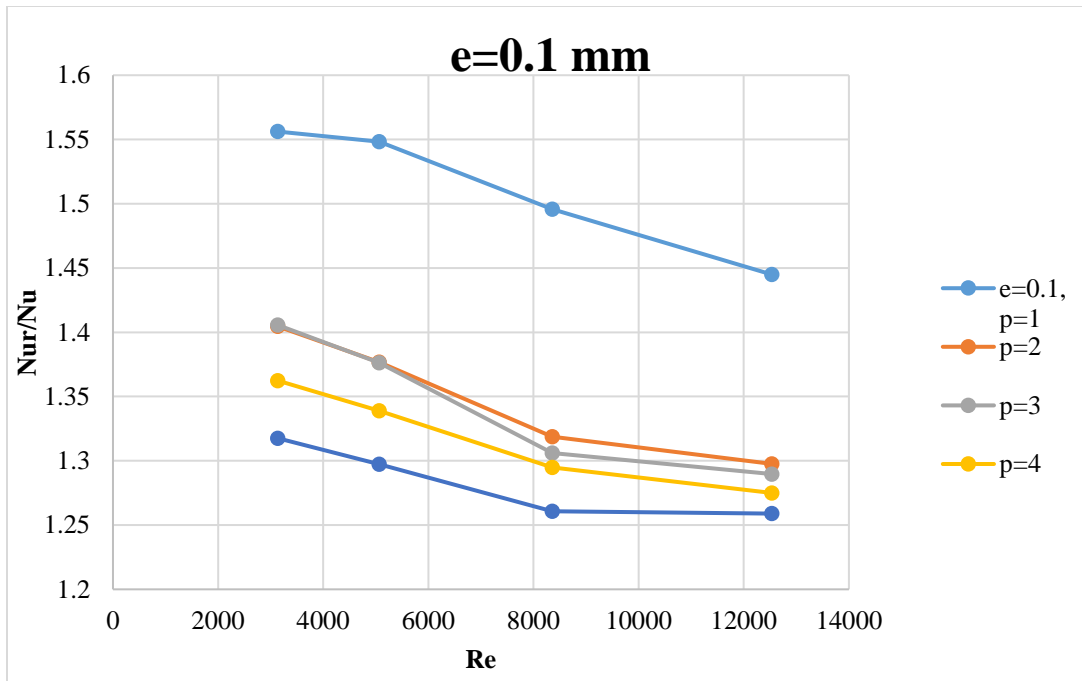


Figure 4.5: Variation of the average Nusselt number ratio with Reynolds number for a fixed value of  $e=0.1$  mm and different values of  $p$  (in mm).

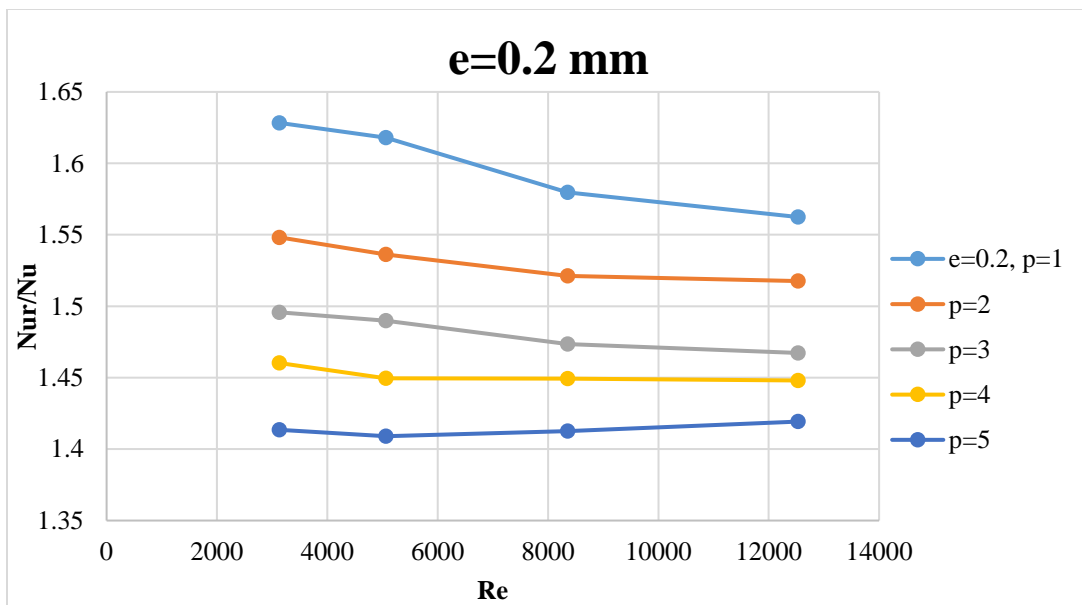


Figure 4.6: Variation of the average Nusselt number ratio with Reynolds number for a fixed value of  $e=0.2$  mm and different values of  $p$  (in mm).

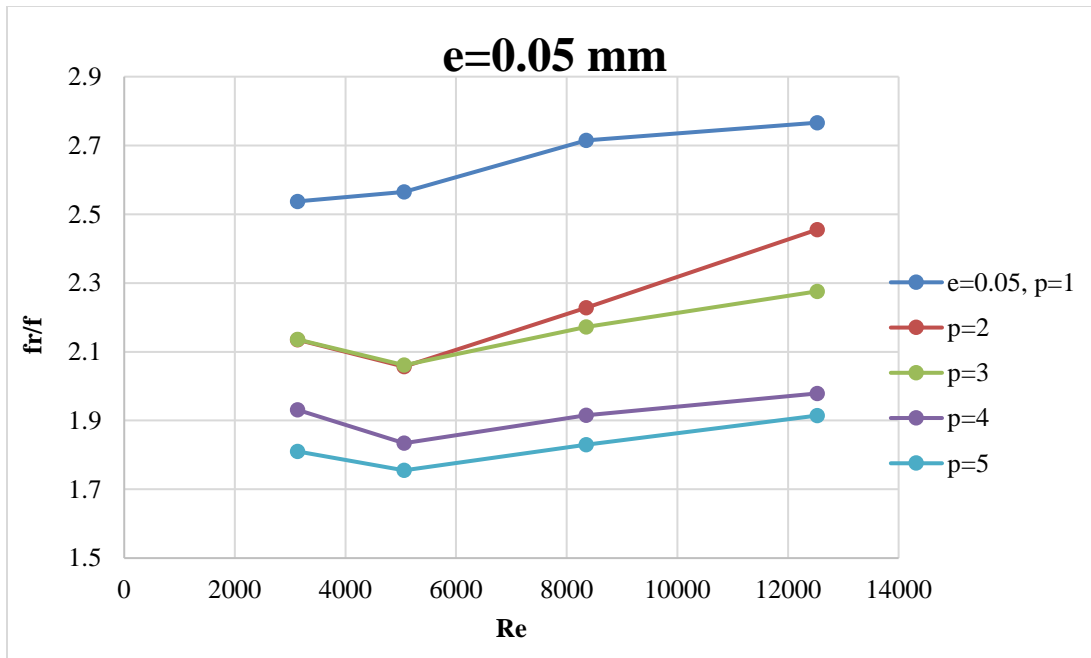


Figure 4.7: Variation of the average friction ratio with Reynolds number for a fixed value of  $e=0.05$  mm and different values of  $p$  (in mm).

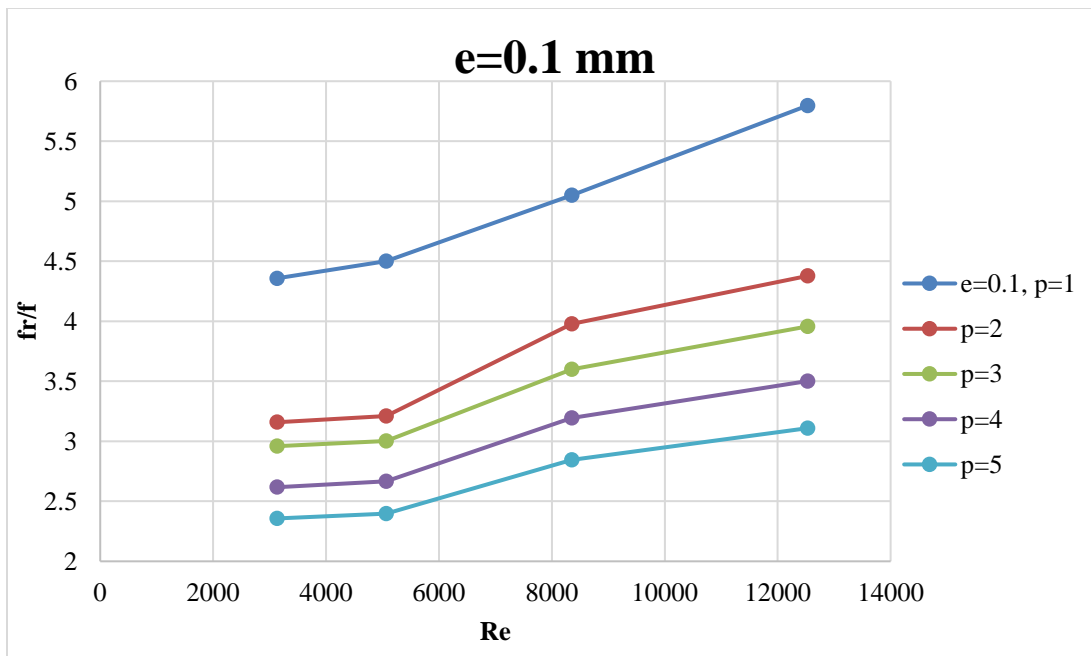


Figure 4.8: Variation of the average friction ratio with Reynolds number for a fixed value of  $e=0.1$  mm and different values of  $p$  (in mm).

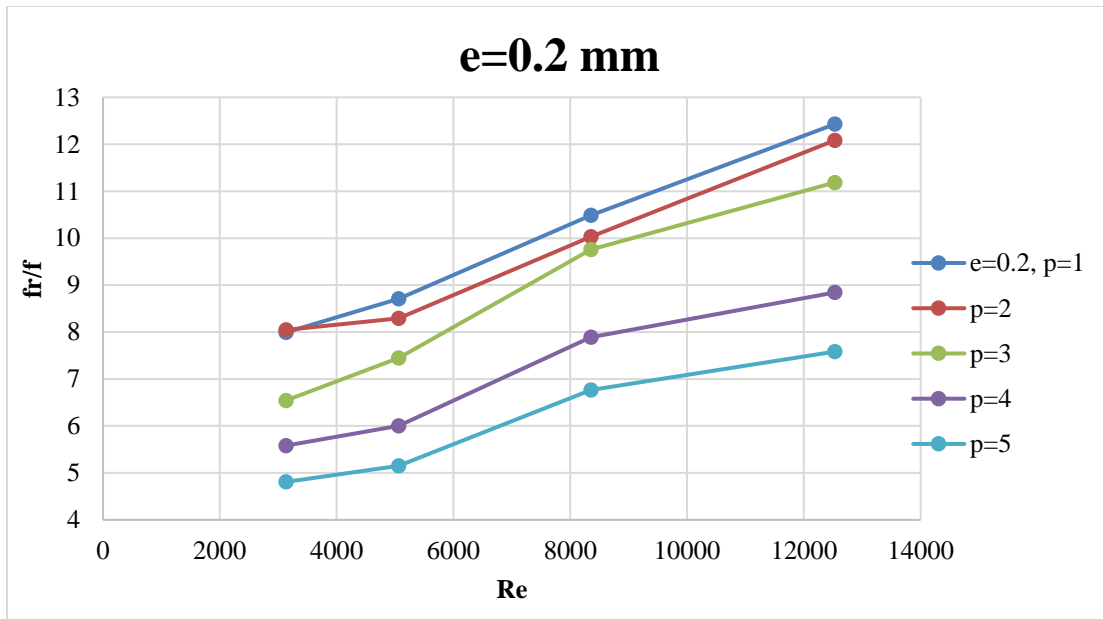


Figure 4.9: Variation of the average friction ratio with Reynolds number for a fixed value of  $e=0.2$  mm and different values of  $p$  (in mm).

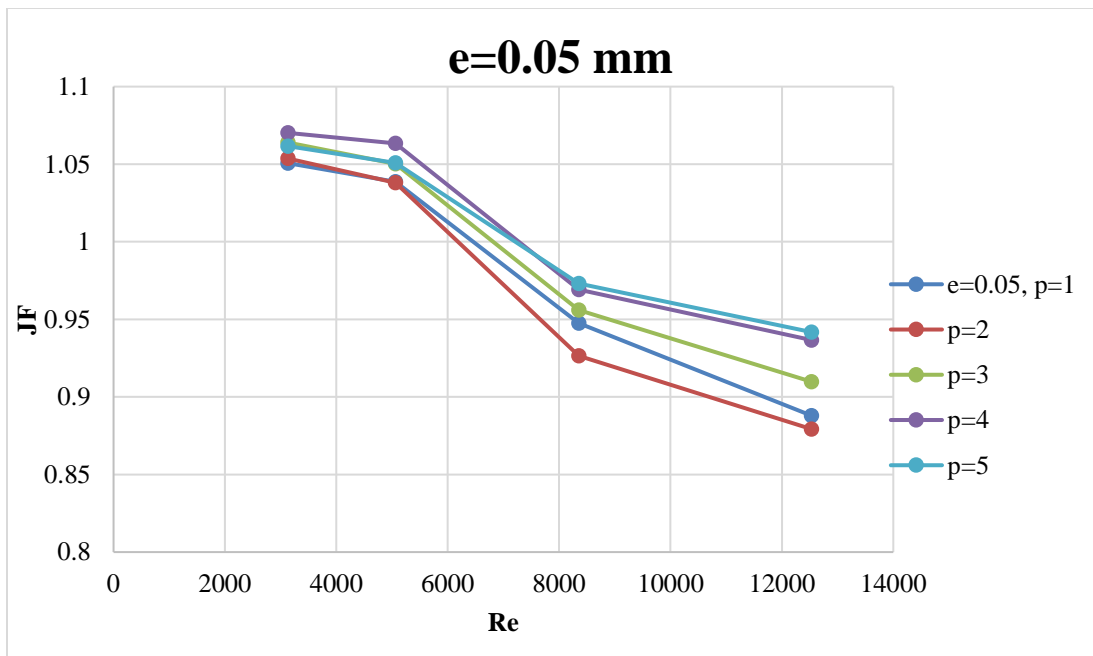


Figure 4.10: Variation of the thermal-hydraulic performance with Reynolds number for a fixed value

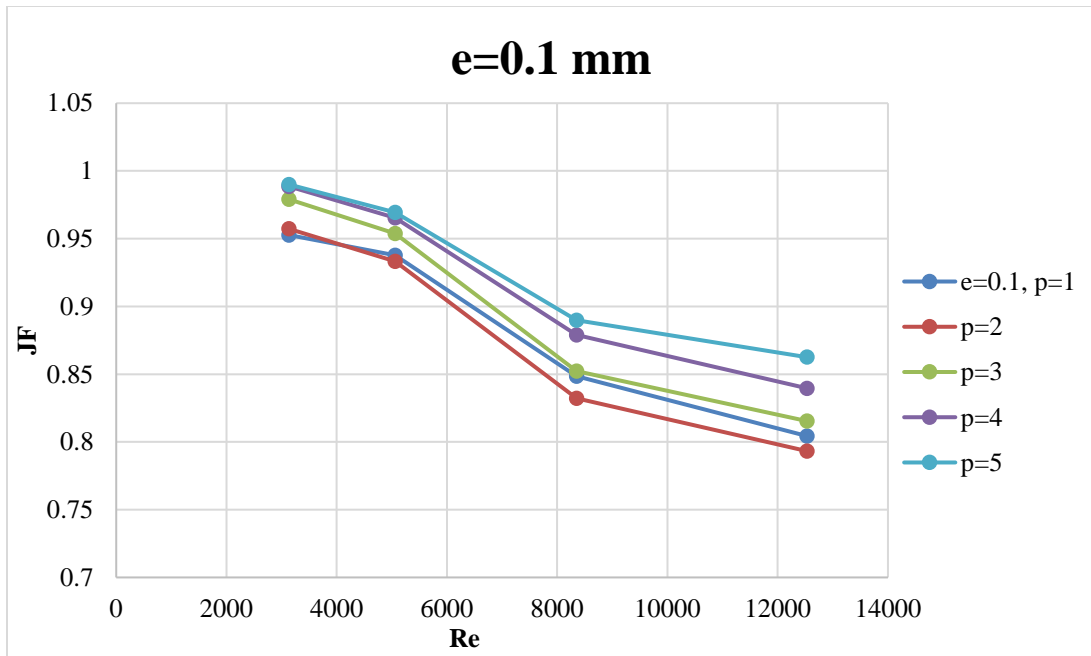


Figure 4.11: Variation of the thermal-hydraulic performance with Reynolds number for a fixed value of  $e=0.1$  mm and different values of  $p$  (in mm).

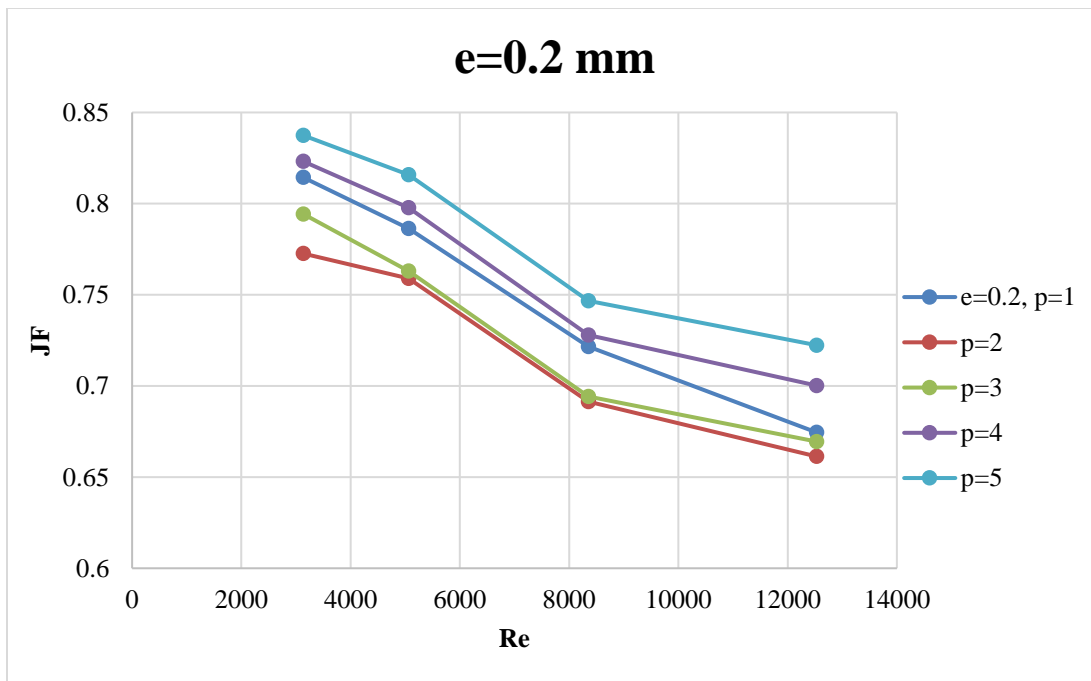


Figure 4.12: Variation of the thermal-hydraulic performance with Reynolds number for a fixed value of  $e=0.2$  mm and different values of  $p$  (in mm).

Figs. 4.10 - 4.12 illustrate the thermal-hydraulic performance ratio ( $JF$ ) of the heat sink at the same pumping power with different Reynolds numbers. The general trend on the three figures is that  $JF$  decreases as Reynolds number increases. This is due to that the increase in pressure drop is much higher than increase in Nusselt number. Fig. 4.10 shows that at  $e=0.05$  mm and  $Re < 8200$ , the highest value of  $JF$  occurs at  $p=4$  mm and for  $Re > 8200$  the highest value occurs at  $p=5$  mm. The lowest value on both cases happens at  $p=2$  mm. similarly, Fig. 4.11 and Fig. 4.12 show that the highest value of  $JF$  occurs at  $p=5$  mm and the lowest value at  $p=2$  mm. The highest  $JF$  value out of all the transverse cases at  $W_{ch}=2$  mm in this study was 1.07 at  $e=0.05$  mm,  $p=4$  mm, and  $Re=3133$  which means only 7% enhancement is obtained. This set of cases is suitable for increasing the rate of heat transfer while ignoring the pressure drop penalty. However, that was not the intention from the beginning; therefore, different parameters are tested to get a better thermal-hydraulic performance.

#### 4.2.1.1 Correlations for Nusselt Number and Friction Factor

Nusselt number and friction factor are significant functions of flow roughness and flow parameters. General correlations are required to cover the following parameters:  $(\frac{e}{D})$  and  $(\frac{P}{D})$ . The constants and exponents in Eq. 4.1 (the correlation parameters) are estimated using nonlinear regression by statistical fitting of the numerical data. The correlations are checked against the average values calculated from the CFD data to find the error. Furthermore, the error is calculated by taking the absolute difference between the CFD and the correlated value of Nu as predicted by Eq. 4.1 and 4.2 and dividing the answer by the

CFD value. From the errors, it is concluded that the correlation works well. This correlation has generally good agreement with the computational data with maximum deviation from the numerical results of 7% as shown in Fig. 4.13.

$$Nu = 0.1868(Re)^{0.8} \left(\frac{P}{D}\right)^{-0.0765} \left(\frac{e}{D}\right)^{0.0978} \quad (4.1)$$

$$f = 0.1276 (Re)^{-0.2} \left(\frac{P}{D}\right)^{-0.27} \left(\frac{e}{D}\right)^{1.046} \quad (4.2)$$

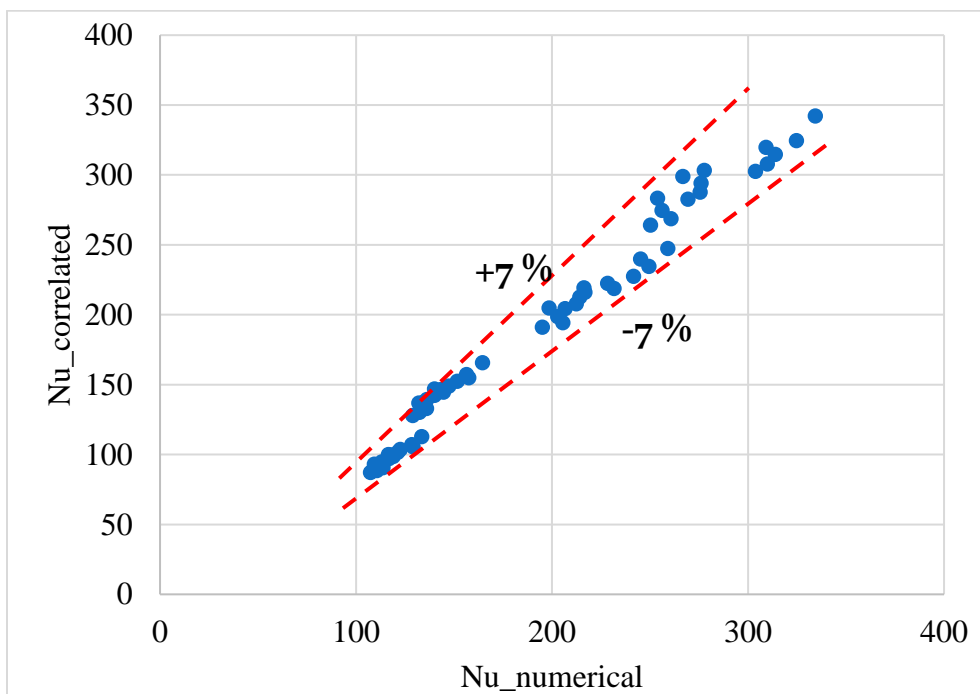


Figure 4.13: Evaluation of the average Nusselt number correlation

#### 4.2.2 Effect of the Inline Ribs

For very narrow channels, the thermal boundary layer encompasses the whole channel width and the effect of boundary layer disturbance using ribs on enhancing the heat transfer coefficient is limited. The heat transfer rate increase for narrow channels is mainly due to the increase in heat transfer area. For wide ribbed channels, both the heat

transfer coefficient and the heat transfer area increase by installing ribs. Therefore, an inline ribs configuration at  $W_{ch} = 6$  mm is proposed in seven different opening ratio (10% - 70%). The proposed configurations are investigated at two different Reynolds numbers (7120 and 28,481) and two different pitches ( $p = 1$  mm and 5 mm).

Figure 4.14 compares the ratio of the average Nusselt number with ribs to the average Nusselt number of the smooth case at different opening ratios at  $p = 5$  mm. It is clear that at a lower Reynolds number, the plot shows a better average Nusselt number ratio. This ratio declines monotonously with climbs in the opening ratio and that's due to the reduction of the rib's weight and the flow velocity; therefore, reduction in the heat transfer area has a proportional relationship with the heat transfer rate. Similarly at  $p = 1$  mm, Fig. 4.17 shows the same trend but at a higher average Nusselt number ratio value due to the smaller ribs pitch on this case. Heat transfer enhances to that of the smooth case by about 37% and 50% at  $p = 5$  mm and  $p = 1$  mm, respectively.

Figures. 4.15 and 4.18 compare the ratio of the average friction with ribs to the average friction with the smooth case at different opening ratio at  $p = 1$  mm and 5 mm. It is obvious that for both figures the ratio is decreasing as the opening ratio increase, and that's due to the reduction in the pressure drop through the opening spaces. Similar to Fig. 4.14 and Fig. 4.17 the average friction ratio decreases as the opening ratio increases.

Figures 4.16 and 4.19 compare the thermal-hydraulic performance for different opening ratios at two different pitches. Both cases show that the thermal-hydraulic increases as the



opening ratio increases up to 50%, which has the highest thermal-hydraulic performance of 1.18 at  $Re=7120$  and  $p=5$  mm, and 1.22 at  $Re=7120$  and  $p=1$  mm. These simulation results show that with proper channel and ribs configuration, one can achieve an increase of about 22% in the thermal-hydraulic performance ratio over that of the smooth channel.

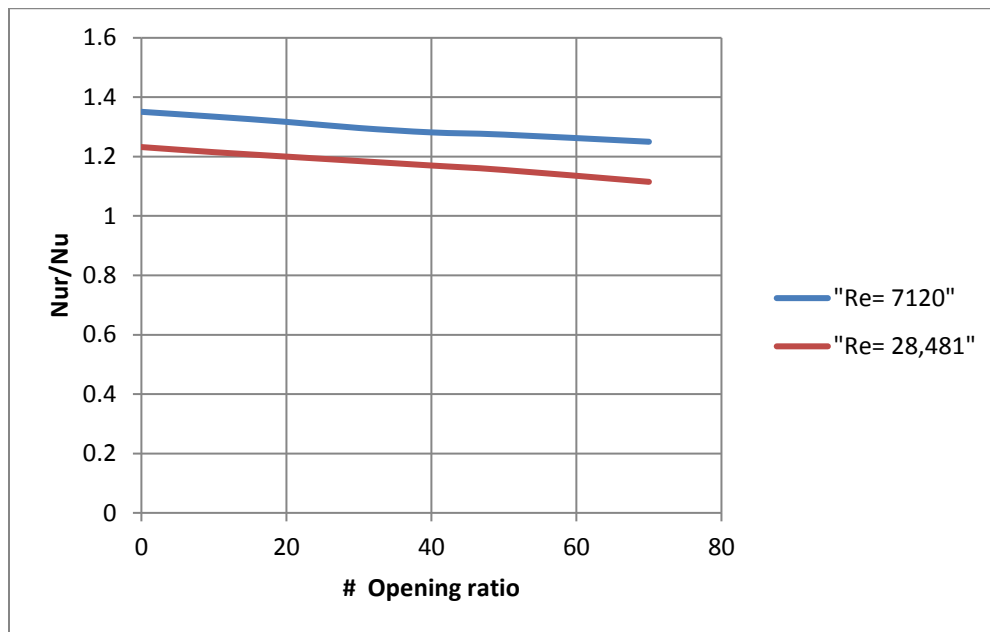


Figure 4.14: Variation of the average Nusselt number ratio with the opening ratio at  $P=5$  mm and two different Reynolds numbers.

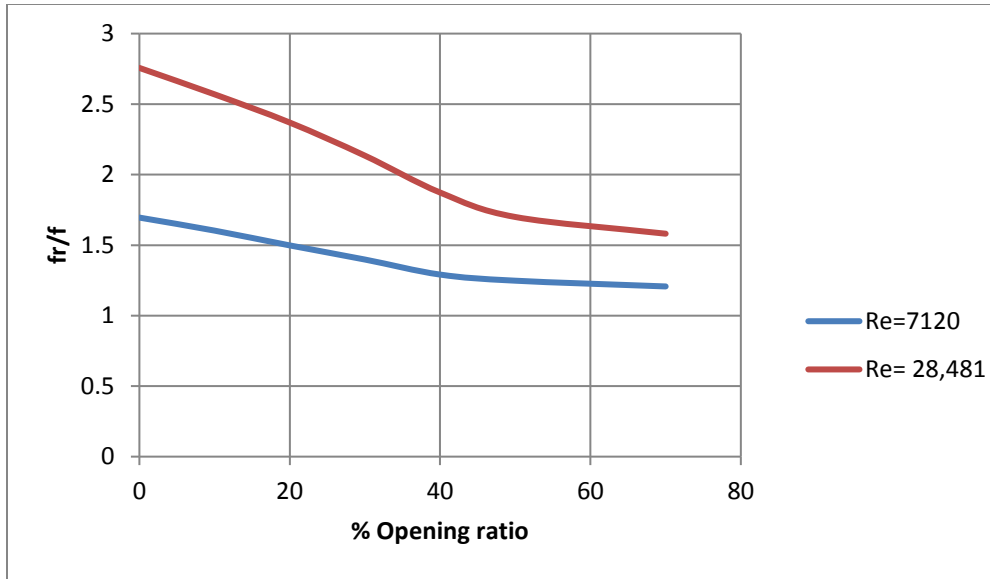


Figure 4.15: Variation of the average friction ratio with the opening ratio at P=5 mm and two different Reynolds numbers.

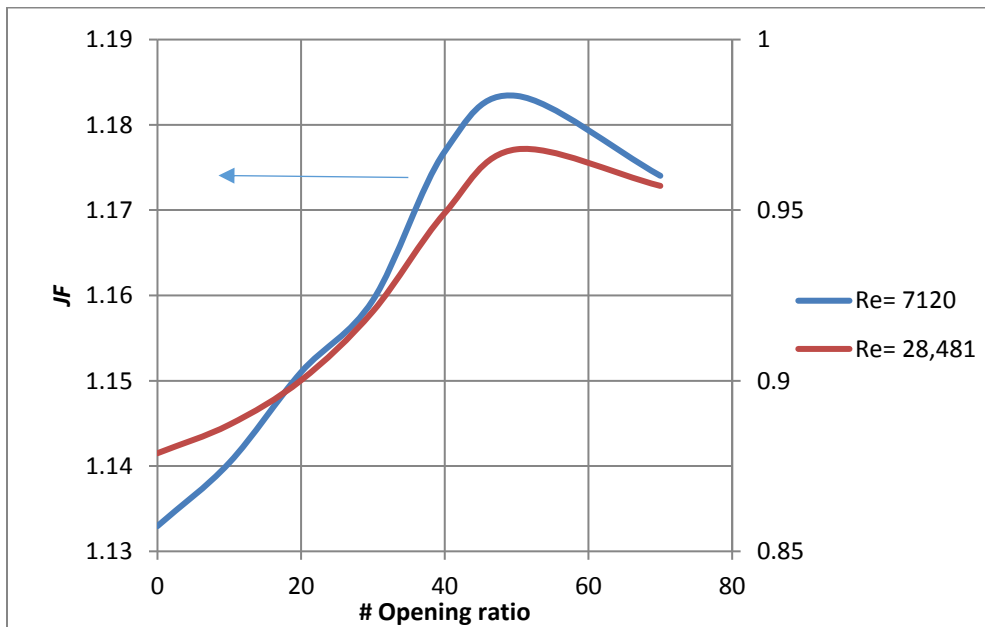


Figure 4.16: Variation of the thermal-hydraulic performance ratio with the opening ratio at P=5 mm and two different Reynolds numbers.

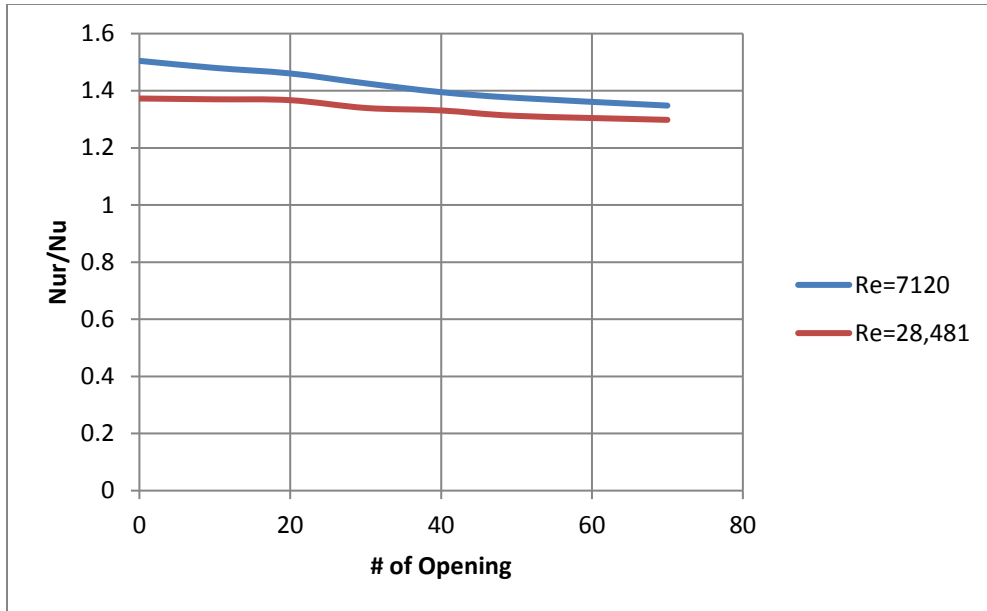


Figure 4.17: Variation of the average Nusselt number ratio with the opening ratio at  $P=1$  mm and two different Reynolds numbers.

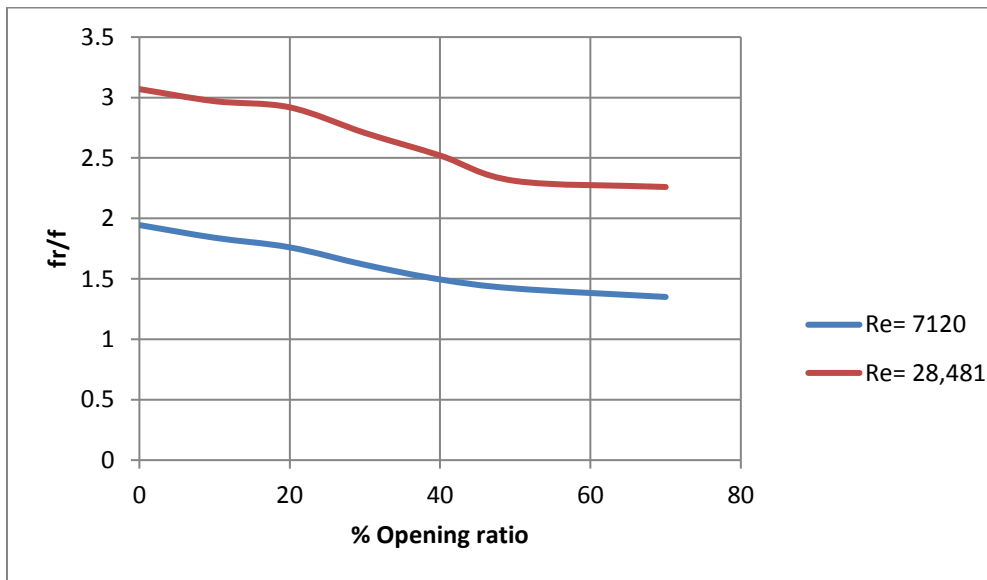


Figure 4.18: Variation of the average friction ratio with the opening ratio at  $P=1$  mm and two different Reynolds numbers.

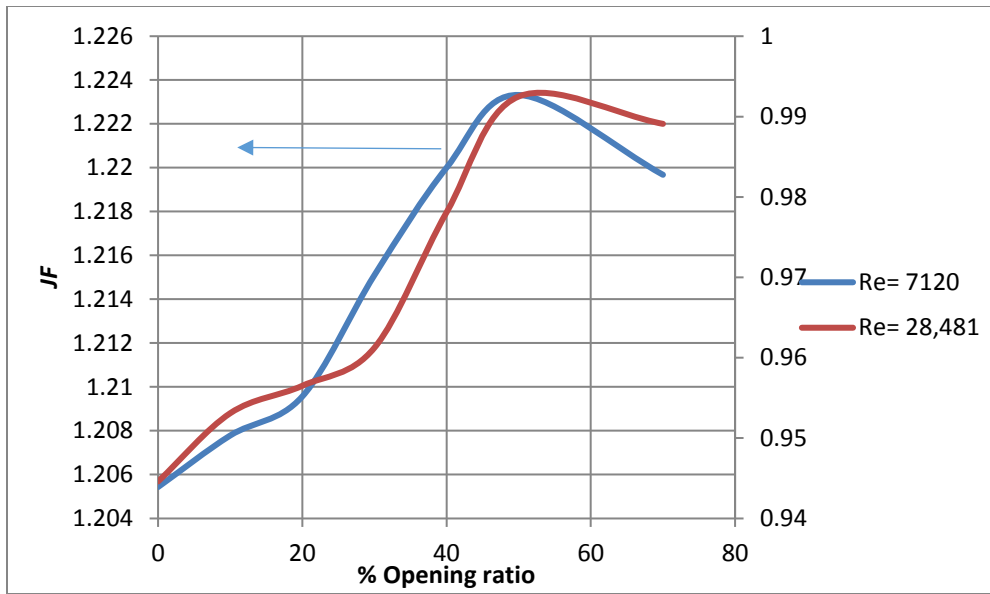


Figure 4.19: Variation of the thermal-hydraulic performance ratio with the opening ratio at P=1 mm and two different Reynolds numbers.

## CHAPTER 5 CONCLUSION

The thermal performance of every component of the electric motor system, including the heats sink, is considered to be critical in order to meet the ever increasing demands of reliability of advanced electric motor cooling systems. Heat transfer through air-cooling can primarily be enhanced by increasing the mass flow rate or the total surface area, or both. Furthermore, the usage of fans or blowers enhances the heat transfer, yet, the pressure drop along the flow increases. This of course results in high instability, augmented acoustical noise and overall cost of the system.

An extensive investigation is performed on this thesis for discussing briefly some of the major design parameters that can be considered for designing an electric motor cooling system (i.e. heat sinks). The most common type of heat sink design is the parallel plate heat sink. However, the main downside of this design is the development of the thermal boundary layer along the length of the fin.

A numerical study on the thermal-hydraulic performance of a parallel plate heat sink mounted on the motor casing is used for the electric motor cooling system. The numerical study is analyzed using ANSYS V.16 to simulate a three dimensional, steady, viscous, turbulent flow model. It also discusses the effect of the different heat sinks' parameters on the heat transfer and pressure drop across the system for uniform heat flux. One of the objectives of this study is to examine the effect of the heat sink geometry on the thermal-

hydraulic performance of the system. The conjugate heat transfer problem is simulated for all the numerical models. To validate the numerical results, experimental available results from a previous work [22] are used.

The thermal-hydraulic performance of plate-fin heat sinks undergoing cross-flow cooling is studied numerically at four different Reynolds numbers, rib heights, rib pitches, rib configurations, and rib opening ratios (OR). Based on the results of this study and the analysis of the impact of the controlling parameters, as well as the optimization study in the previous chapters, the following conclusions are drawn:

1. Pressure drop and heat transfer increase significantly with a decrease in rib spacing for the same volumetric flow rate.
2. Increasing rib height increases the pressure drop and the heat transfer for the same flow rate.
3. In the continuous ribs, the average Nusselt number ratio decreases as Reynolds number increases. Rib pitch of 1 mm produces the highest average Nusselt number ratio for the three rib heights.
4. The highest average Nusselt number ratio among the continuous rib cases occurs at the case where  $e=0.2$  mm,  $p=1$  mm, and  $Re=3133$ . This ribbed case increases the Nusselt number by about 63% over that of the base smooth case.

5. The friction factor ratio increases when Reynolds number increases and heat sinks of 1mm pitch have the highest value of 12.4 mm times higher than the smooth base case at  $e=0.2$  mm and  $p=1$  mm.
6. The thermal-hydraulic performance ( $JF$ ) decreases as Reynolds number increases. At lower Reynolds number, the less ribs added to the fins the better  $JF$  one will get, and vice versa for the higher Reynolds number.
7. The highest ( $JF$ ) value out of all the continuous ribs cases at  $W_{ch}=2$  mm in this study is 1.07 at  $e=0.05$  mm,  $p=4$  mm, and  $Re=3132.91$  which means only 7% enhancement is obtained. This set of cases is suitable for increasing the rate of heat transfer while ignoring the pressure drop penalty
8. Flow and heat correlations are obtained to ease the calculation of the effect of the two parameters  $(\frac{e}{D})$  and  $(\frac{P}{D})$ .
9. To reduce the amount of pressure drop, an inline ribs configuration is proposed in seven different opening ratios (10% - 70%) at  $W_{ch}=6$ mm.
10. It is clear that at lower Reynolds numbers, the result shows a better average Nusselt number ratio. This ratio declines monotonously with climbs in the ribs opening ratio.
11. At the case where  $e=0.2$  mm and  $Re=7120$ , heat transfer enhances to that of the smooth case by about 37% at  $p=5$  mm and 50% at  $p=1$  mm.
12. At  $W_{ch}=6$  mm, the ratio of the average friction with ribs to the average friction with

the smooth case is decreasing as the opening ratio increases, and that is due to the reduction in the pressure drop through the opening spaces.

13. A comparison of the thermal-hydraulic performance for different opening ratios at two different pitches is obtained. Both cases show that the thermal-hydraulic increases with increasing the opening ratio up to 50% which has the highest thermal-hydraulic performance of 1.18 at  $Re=7120$  and  $p=5$  mm, and 1.22 and at  $Re=7120$  and  $p=1$  mm.
14. These simulation results show that with proper channel and ribs configuration, one can achieve an increase of about 22% in the thermal-hydraulic performance ratio over that of the smooth channel.



## LIST OF REFERENCES

- [1] WaIde, P., & Brunner, C. U. (2011). Energy-efficiency policy opportunities for electric motor-driven systems.
- [2] Malcolm, D. R. (2006). Turn energy waste into profit. Plant services, <http://www.plantservices.com/articles/2006/313/?show=all>.
- [3] Scheihing, P. E. (2007). A national strategy for energy efficient industrial motor-driven systems. In *Energy Efficiency Improvement in Electric Motors and Drives. Part VIII*, Springer, Berlin Heidelberg, pp. 377–389.
- [4] Tong, W. (2014). *Mechanical design of electric motors*. CRC Press.
- [5] Venkataraman, B., Godsey, B., Premerlani, W., Shulman, E., Thaku, M., & Midence, R. (2005, April). Fundamentals of a motor thermal model and its applications in motor protection. In *58th Annual Conference for Protective Relay Engineers*, (pp. 127-144).
- [6] Motor Reliability Working Group. (1985). Report of large motor reliability survey of industrial and commercial installations, Part I. *IEEE Transactions of Industry Applications* IA-21(4): 853–864.
- [7] Motor Reliability Working Group. (1985). Report of large motor reliability survey of industrial and commercial installations, Part II. *IEEE Transactions of Industry Applications* IA-21(4): 865–872.

- [8] Motor Reliability Working Group. (1987). Report of large motor reliability survey of industrial and commercial installations, Part III. *IEEE Transactions of Industry Applications* IA-23(1): 153–158.
- [9] Cornell, E. P., Owen, E. L., Appiarius, J. C., McCoy, R. M., Albrecht, P. F., & Houghtaling, D. W. (1982). *Improved motors for utility applications. Final report* (No. EPRI-EL-2678-Vol. 1). General Electric Co., Schenectady, NY (USA).
- [10] Tong, W. (2001). Numerical analysis of rotating pumping flows in inter-coil rotor cavities and short cooling grooves of a generator. *International Journal of Rotating Machinery*, 7(2), 131-141.
- [11] Benhaddadi, M., Olivier, G., Yelle, J., Tremblay, J. F., & Ibtouen, R. (2011). *Premium Efficiency Motors*. INTECH Open Access Publisher.
- [12] GE Industrial Systems. (2002). Evaluation and application of energy efficient motors. White paper publication number: e-GEA-M1019. <http://www.geindustrial.com/publibrary/checkout/e-GEA-M1019?TNR=WhitePapers|e-GEA-M1019|generic>
- [13] Meyer IV, G. A., Sun, C. H., Chen, C. P., & Liu, H. T. (2011). *U.S. Patent No. 8,059,406*. Washington, DC: U.S. Patent and Trademark Office.
- [14] Mudawar, I. (2001). Assessment of high-heat-flux thermal management schemes. *IEEE Transactions on Components and Packaging Technologies*, 24(2), 122-141.

- [15] Yeh, L.T., 1995, "Review of heat transfer technologies in electronic equipment", ASME J. Electron. Packag. 117, pp.333-339.
- [16] Lee, S. (1995). Optimum design and selection of heat sinks. In *Semiconductor Thermal Measurement and Management Symposium, 1995. SEMI-THERM XI., Eleventh Annual IEEE* (pp. 48-54). IEEE.
- [17] <https://www.aavid.com/sites/default/files/literature/Thermal-Solutions-Brochure.pdf>
- [18] Bergman, T. L., Incropera, F. P., DeWitt, D. P., & Lavine, A. S. (2011). *Fundamentals of Heat and Mass Transfer, 6<sup>th</sup> Edition*. John Wiley & Sons.
- [19] Kraus, A. D., & Bar-Cohen, A. (1983). Thermal analysis and control of electronic equipment. *Washington, DC, Hemisphere Publishing Corp., 1983, 633 p., 1.*
- [20] Han, J. C. (1984). Heat transfer and friction in channels with two opposite rib-roughened walls. *Journal of Heat Transfer, 106(4), 774-781.*
- [21] Han, J. C., Park, J. S., & Lei, C. K. (1985). Heat transfer enhancement in channels with turbulence promoters. *Journal of Engineering for Gas Turbines and Power, 107(3), 628-635.*
- [22] Han, J. C., & Park, J. S. (1988). Developing heat transfer in rectangular channels with rib turbulators. *International Journal of Heat and Mass Transfer, 31(1), 183-195.*
- [23] Lau, S. C., McMillin, R. D., & Han, J. C. (1991). Turbulent heat transfer and friction in a square channel with discrete rib turbulators. *Journal of turbomachinery, 113(3), 360-366.*

- [24] Didarul, I. M., Kenyu, O., Minoru, Y., & Izuru, S. (2007). Study on heat transfer and fluid flow characteristics with short rectangular plate fin of different pattern. *Experimental Thermal and Fluid Science*, 31(4), 367-379.
- [25] Prasad, K., & Mullick, S. C. (1983). Heat transfer characteristics of a solar air heater used for drying purposes. *Applied Energy*, 13(2), 83-93.
- [26]. Prasad, B. N., & Saini, J. S. (1988). Effect of artificial roughness on heat transfer and friction factor in a solar air heater. *Solar energy*, 41(6), 555-560.
- [27] Gupta, D., Solanki, S. C., & Saini, J. S. (1997). Thermohydraulic performance of solar air heaters with roughened absorber plates. *Solar Energy*, 61(1), 33-42.
- [28] Verma, S. K., & Prasad, B. N. (2000). Investigation for the optimal thermohydraulic performance of artificially roughened solar air heaters. *Renewable Energy*, 20(1), 19-36.
- [29] Momin, A. M. E., Saini, J. S., & Solanki, S. C. (2002). Heat transfer and friction in solar air heater duct with V-shaped rib roughness on absorber plate. *International journal of heat and mass transfer*, 45(16), 3383-3396.
- [30] Hans, V. S., Saini, R. P., & Saini, J. S. (2010). Heat transfer and friction factor correlations for a solar air heater duct roughened artificially with multiple v-ribs. *Solar Energy*, 84(6), 898-911.
- [31]. Sriromreun, P., Thianpong, C., & Promvonge, P. (2012). Experimental and numerical study on heat transfer enhancement in a channel with Z-shaped baffles. *International Communications in Heat and Mass Transfer*, 39(7), 945-952.

- [32] Promvonge, P., Sripattanapipat, S., & Kwankaomeng, S. (2010). Laminar periodic flow and heat transfer in square channel with 45 inline baffles on two opposite walls. *International Journal of Thermal Sciences*, 49(6), 963-975.
- [33] Mohammadi, K., & Sabzpooshani, M. (2013). Comprehensive performance evaluation and parametric studies of single pass solar air heater with fins and baffles attached over the absorber plate. *Energy*, 57, 741-750.
- [34] Goldberg, N. (1984). Narrow channel forced air heat sink. *IEEE transactions on components, hybrids, and manufacturing technology*, 7(1), 154-159.
- [35] Mansuria, M. S., & Kamath, V. (1994). Design optimization of a high-performance heat-sink/fan assembly. *ASME-PUBLICATIONS-HTD*, 292, 95-95.
- [36] Sathyamurthy, P., Runstadler, P. W., & Lee, S. (1996, May). Numerical and experimental evaluation of planar and staggered heat sinks. In *Thermal Phenomena in Electronic Systems, 1996. I-THERM V., Inter-Society Conference on* (pp. 132-139). IEEE.
- [37] Teertstra, P., Yovanovich, M. M., & Culham, J. R. (2000). Analytical forced convection modeling of plate fin heat sinks. *Journal of Electronics Manufacturing*, 10(04), 253-261..
- [38] El-Sayed, S. A., Mohamed, S. M., Abdel-latif, A. A., & Abdel-hamid, E. A. (2004). Experimental study of heat transfer and fluid flow in longitudinal rectangular-fin array located in different orientations in fluid flow. *Experimental Thermal and Fluid Science*, 29(1), 113-128.

- [39] Kim, S. J., Kim, D. K., & Oh, H. H. (2008). Comparison of fluid flow and thermal characteristics of plate-fin and pin-fin heat sinks subject to a parallel flow. *Heat Transfer Engineering*, 29(2), 169-177..
- [40]. Li, H. Y., & Chao, S. M. (2009). Measurement of performance of plate-fin heat sinks with cross flow cooling. *International Journal of Heat and Mass Transfer*, 52(13), 2949-2955.
- [41] Ahmed, H. E. (2016). Optimization of thermal design of ribbed flat-plate fin heat sink. *Applied Thermal Engineering*, 102, 1422-1432.
- [42] Mohammadi, K., & Sabzpooshani, M. (2013). Comprehensive performance evaluation and parametric studies of single pass solar air heater with fins and baffles attached over the absorber plate. *Energy*, 57, 741-750.
- [43] Moharana, M. K., Agarwal, G., & Khandekar, S. (2011). Axial conduction in single-phase simultaneously developing flow in a rectangular mini-channel array. *International Journal of Thermal Sciences*, 50(6), 1001-1012.
- [44] Mohammed, H. A., Gunnasegaran, P., & Shuaib, N. H. (2011). The impact of various nanofluid types on triangular microchannels heat sink cooling performance. *International Communications in Heat and Mass Transfer*, 38(6), 767-773.
- [45] Sharma, C. S., Tiwari, M. K., Michel, B., & Poulikakos, D. (2013). Thermofluidics and energetics of a manifold microchannel heat sink for electronics with recovered

- hot water as working fluid. *International Journal of Heat and Mass Transfer*, 58(1), 135-151.
- [46] Wang, H., Chen, Z., & Gao, J. (2016). Influence of geometric parameters on flow and heat transfer performance of micro-channel heat sinks. *Applied Thermal Engineering*, 107, 870-879.
- [47] Saeed, M., & Kim, M. H. (2016). Numerical study on thermal hydraulic performance of water cooled mini-channel heat sinks. *International Journal of Refrigeration*.
- [48] Vermahmoudi, Y., Peyghambarzadeh, S. M., Hashemabadi, S. H., & Naraki, M. (2014). Experimental investigation on heat transfer performance of/water nanofluid in an air-finned heat exchanger. *European Journal of Mechanics-B/Fluids*, 44, 32-41..
- [49] Mohammed, H. A., Hasan, H. A., & Wahid, M. A. (2013). Heat transfer enhancement of nanofluids in a double pipe heat exchanger with louvered strip inserts. *International Communications in Heat and Mass Transfer*, 40, 36-46.
- [50] Xia, G. D., Liu, R., Wang, J., & Du, M. (2016). The characteristics of convective heat transfer in microchannel heat sinks using  $Al_2O_3$  and  $TiO_2$  nanofluids. *International Communications in Heat and Mass Transfer*, 76, 256-264.
- [51] Ahmed, H. E., Ahmed, M. I., Seder, I. M., & Salman, B. H. (2016). Experimental investigation for sequential triangular double-layered microchannel heat sink with nanofluids. *International Communications in Heat and Mass Transfer*, 77, 104-115.

- [52] Aung, W. (1988). *Cooling technology for electronic equipment* (No. CONF-8703288-). New York, NY; Hemisphere Publishing..
- [53] Deans, J., Neale, J., Dempster, W., & Lee, C. K. (2006). The use of effectiveness concepts to calculate the thermal resistance of parallel plate heat sinks. *Heat transfer engineering*, 27(5), 56-67..
- [54] Wu, H. H., Hsiao, Y. Y., Huang, H. S., Tang, P. H., & Chen, S. L. (2011). A practical plate-fin heat sink model. *Applied Thermal Engineering*, 31(5), 984-992.
- [55] Ahn, S. W., & Son, K. P. (2002). An investigation on friction factors and heat transfer coefficients in a rectangular duct with surface roughness. *KSME international journal*, 16(4), 549-556.
- [56] Srivastav, A., Patil, A. K., & Nandan, G. (2014). Investigation of heat transfer and friction in rib roughened fin under forced convection. In *International Journal of Advanced Technology & Engineering Research (IJATER) 1st International Conference on Research in Science, Eng. Manag.(IOCRSEM 2014)* (pp. 117-125).
- [57] Bassiouny, R., Maher, H., & Hegazy, A. A. (2016). On the thermal analysis of a plate-fin heat sink considering the thermal-entry length effect. *Applied Thermal Engineering*, 99, 273-279.
- [58] Moawed, M. (2011). Experimental study of forced convection from helical coiled tubes with different parameters. *Energy Conversion and Management*, 52(2), 1150-1156.



- [59] Aly, W. I. (2014). Numerical study on turbulent heat transfer and pressure drop of nanofluid in coiled tube-in-tube heat exchangers. *Energy Conversion and Management*, 79, 304-316.
- [60] Eiamsa-ard, S., Pethkool, S., Thianpong, C., & Promvonge, P. (2008). Turbulent flow heat transfer and pressure loss in a double pipe heat exchanger with louvered strip inserts. *International Communications in Heat and Mass Transfer*, 35(2), 120-129.
- [61] Kotcioglu, I., Caliskan, S., Cansiz, A., & Baskaya, S. (2010). Second law analysis and heat transfer in a cross-flow heat exchanger with a new winglet-type vortex generator. *Energy*, 35(9), 3686-3695.
- [62] Torii, K., Kwak, K. M., & Nishino, K. (2002). Heat transfer enhancement accompanying pressure-loss reduction with winglet-type vortex generators for fin-tube heat exchangers. *International Journal of Heat and Mass Transfer*, 45(18), 3795-3801.
- [63] Han, H., Li, B., & Shao, W. (2014). Multi-objective optimization of outward convex corrugated tubes using response surface methodology. *Applied Thermal Engineering*, 70(1), 250-262.
- [64] Garcia, A., Solano, J. P., Vicente, P. G., & Viedma, A. (2012). The influence of artificial roughness shape on heat transfer enhancement: Corrugated tubes, dimpled tubes and wire coils. *Applied Thermal Engineering*, 35, 196-201.

- [65] Rainieri, S., & Pagliarini, G. (2002). Convective heat transfer to temperature dependent property fluids in the entry region of corrugated tubes. *International Journal of Heat and Mass Transfer*, 45(22), 4525-4536.
- [66] Esmaeilzadeh, E., Almohammadi, H., Nokhosteen, A., Motezaker, A., & Omrani, A. N. (2014). Study on heat transfer and friction factor characteristics of  $\gamma$ -Al<sub>2</sub>O<sub>3</sub>/water through circular tube with twisted tape inserts with different thicknesses. *International Journal of Thermal Sciences*, 82, 72-83.
- [67] Eiamsa-ard, S., Yongsiri, K., Nanan, K., & Thianpong, C. (2012). Heat transfer augmentation by helically twisted tapes as swirl and turbulence promoters. *Chemical Engineering and Processing: Process Intensification*, 60, 42-48.
- [68] Bhuiya, M. M. K., Chowdhury, M. S. U., Shahabuddin, M., Saha, M., & Memon, L. A. (2013). Thermal characteristics in a heat exchanger tube fitted with triple twisted tape inserts. *International Communications in Heat and Mass Transfer*, 48, 124-132.
- [69] Sahu, M. M., & Bhagoria, J. L. (2005). Augmentation of heat transfer coefficient by using 90 broken transverse ribs on absorber plate of solar air heater. *Renewable Energy*, 30(13), 2057-2073.
- [70] Aharwal, K. R., Gandhi, B. K., & Saini, J. S. (2008). Experimental investigation on heat-transfer enhancement due to a gap in an inclined continuous rib arrangement in a rectangular duct of solar air heater. *Renewable energy*, 33(4), 585-596.

- [71] Singh, S., Chander, S., & Saini, J. S. (2011). Heat transfer and friction factor of discrete V-down rib roughened solar air heater ducts. *Journal of Renewable and Sustainable Energy*, 3(1), 013108.
- [72] Kumar, A., Saini, R. P., & Saini, J. S. (2012). Experimental investigation on heat transfer and fluid flow characteristics of air flow in a rectangular duct with Multi v-shaped rib with gap roughness on the heated plate. *Solar Energy*, 86(6), 1733-1749.
- [73] Lee, R. S., Huang, H. C., & Chen, W. Y. (1990, February). A thermal characteristic study of extruded-type heat sinks in considering air flow bypass phenomenon. In *Semiconductor Thermal and Temperature Measurement Symposium, 1990. SEMI-THERM VI, Proceedings., Sixth Annual IEEE* (pp. 95-102). IEEE.
- [74] Gao, X., & Sundén, B. (2004). Effects of inclination angle of ribs on the flow behavior in rectangular ducts. *Journal of fluids engineering*, 126(4), 692-699.
- [75] Shaeri, M. R., Yaghoubi, M., & Jafarpur, K. (2009). Heat transfer analysis of lateral perforated fin heat sinks. *Applied energy*, 86(10), 2019-2029.
- [76] Layek, A. (2010). Optimal thermo-hydraulic performance of solar air heater having chamfered rib-groove roughness on absorber plate. *International Journal of Energy and Environment*, 1(4), 683-696.
- [77] DO SEO, P. A. R. K. (2007). *Experimental and numerical study of laminar forced convection heat transfer for a dimpled heat sink* (Doctoral dissertation, Texas A&M University).
- [78] Fluent, I. (2006). FLUENT user's guide. *Fluent Inc.*

[79] Ahmed, M. AI-Mogbel. (2004). *Analysis of human thermal comfort using a coupled model for predicting human body-environment heat and mass exchange*, (Doctoral dissertation, *Old Dominion University*)